International Journal of Nanomedicine

Dovepress
Taylor & Francis Group

Open Access Full Text Article

ORIGINAL RESEARCH

Microenvironment-Activated Fe-MOF Nanoplatform Enables Controlled Doxorubicin Release and Ferroptosis-Associated Oxidative Damage in MCF-7 Breast Cancer Cells

Miao Yuan[1,*], Yang Wu[1,*], Jing Zheng[1,*], Chaoran Wang[1], Jiarong Wang[1], Yifan Zheng[1], Yunqi Wang[1], Baiqi Wang[1,2]

[1]Department of Occupational and Environmental Health, School of Public Health, Tianjin Medical University, Tianjin, 300070, People's Republic of China; [2]National Demonstration Center for Experimental Preventive Medicine Education (Tianjin Medical University), Tianjin, 300070, People's Republic of China

*These authors contributed equally to this work

Correspondence: Baiqi Wang, Department of Occupational and Environmental Health, School of Public Health, Tianjin Medical University, No. 22, Qixiangtai Road, Heping Dist, Tianjin, 300070, People's Republic of China, Tel +86-22-83336630, Fax +86-22-83336603, Email wangbaiqi@tmue.edu.cn

---

Introduction: Doxorubicin (DOX) is a cornerstone chemotherapeutic for breast cancer; however, its clinical efficacy is limited by inefficient intracellular delivery and dose-limiting off-target toxicity. Microenvironment-responsive nanoplatforms offer a promising strategy to enhance tumor selectivity and therapeutic performance.

Methods: A core–shell nanosystem (UTMD) was constructed by coating an NH_2-MIL-88B(Fe) metal–organic framework (Fe-MOF) shell onto a UCNP@TiO_2 scaffold. The Fe-MOF shell was designed as a dual pH- and glutathione (GSH)-responsive gatekeeper for controlled DOX release. The nanosystem was characterized for structural features, drug loading, and stimulus-responsive release behavior. Cellular uptake, intracellular trafficking, cytotoxicity, and redox-related biochemical changes were evaluated in MCF-7 breast cancer cells and HEK-293 normal cells.

Results: UTMD achieved high encapsulation efficiency (86.5%) and maintained stability under physiological conditions, while enabling accelerated DOX release in acidic and reducing environments. The nanosystem enhanced cellular internalization and promoted nuclear accumulation of DOX in MCF-7 cells. In addition, UTMD induced significant intracellular redox imbalance, characterized by GSH depletion, increased reactive oxygen species levels, and elevated lipid peroxidation, accompanied by mitochondrial membrane potential depolarization. These changes are consistent with ferroptosis-associated oxidative damage. Compared with free DOX, UTMD exhibited improved cytocompatibility in HEK-293 cells.

Discussion: The Fe-MOF shell functions as a microenvironment-responsive gatekeeper that coordinates controlled drug release with iron-mediated oxidative stress. This integrated design links chemotherapy with ferroptosis-associated mechanisms, improving therapeutic selectivity and mechanistic interpretability.

Conclusion: UTMD represents a microenvironment-activated nanoplatform that enables controlled DOX delivery and ferroptosis-associated oxidative damage. This strategy enhances antitumor efficacy while reducing off-target toxicity, offering potential for improved breast cancer therapy.

Keywords: Fe-based metal–organic framework, pH/GSH-responsive nanoplatform, doxorubicin delivery, ferroptosis, lipid peroxidation, breast cancer

---

Introduction

Breast cancer remains one of the most common malignancies worldwide and a leading cause of cancer-related mortality among women.[1,2] Although breast cancer diagnosis and treatment have advanced considerably, long-term clinical control

https://doi.org/10.2147/IJN.S604452
Received: 21 February 2026
Accepted: 24 April 2026
Published: 1 May 2026

Graphical Abstract

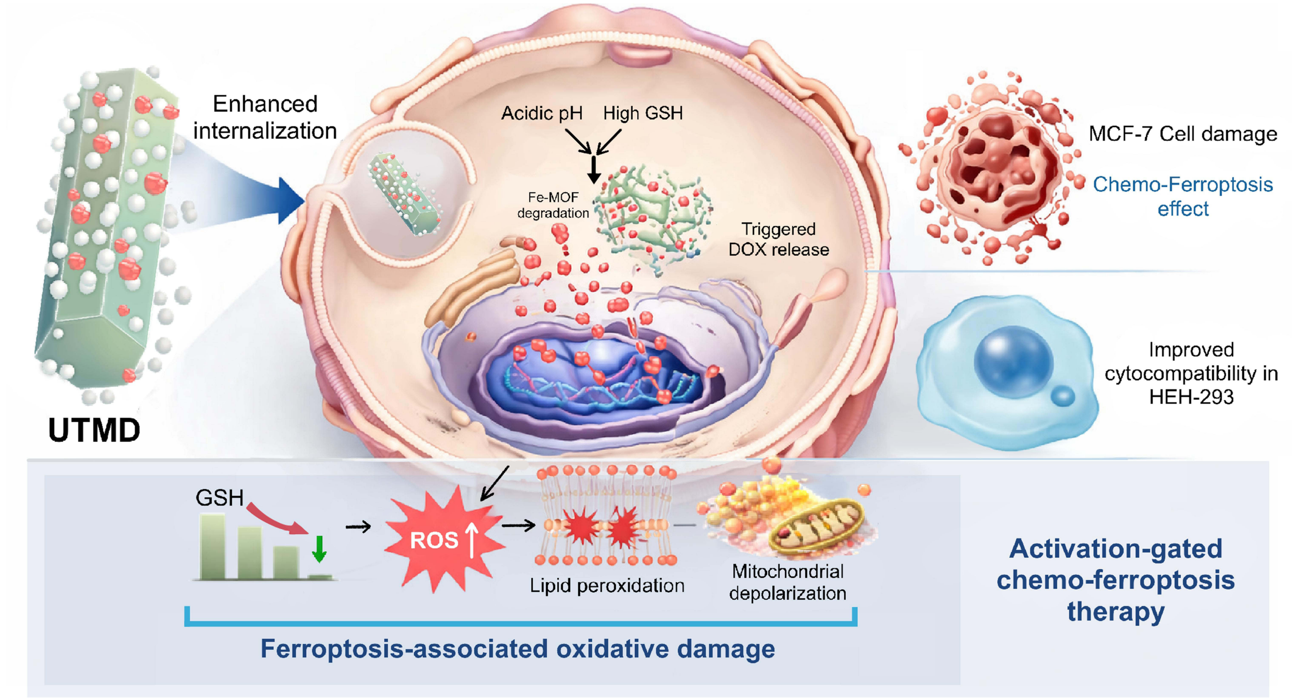

remains limited by recurrence, therapeutic resistance, and insufficient treatment selectivity.[3,4] Doxorubicin (DOX) is a widely used chemotherapeutic agent for breast cancer, but its clinical application is restricted by dose-dependent cardiotoxicity, nonspecific tissue injury, and limited selectivity for tumor cells.[5,6] These challenges have stimulated extensive interest in nanocarrier-based DOX delivery systems.

Conventional DOX nanocarriers, including liposomes, polymeric nanoparticles, micelles, mesoporous silica nanoparticles, and hybrid nanomaterials, can improve drug solubility, prolong circulation time, and reduce systemic toxicity to varying degrees.[7] However, most of these systems primarily function as passive delivery vehicles. Although they can improve pharmacokinetic behavior, they often do not directly address intracellular mechanisms that contribute to tumor cell survival during chemotherapy. In particular, incomplete intracellular drug release and strong antioxidant defenses may limit the cytotoxic effect of DOX even after cellular uptake.[8] Therefore, improving delivery efficiency alone may be insufficient; an effective nanoplatform should ideally combine controlled drug release with a complementary mechanism that increases tumor cell susceptibility to treatment.

One strategy is to exploit biochemical characteristics of the tumor microenvironment as endogenous triggers for intracellular activation. Solid tumors typically exhibit mildly acidic extracellular conditions, with more pronounced acidity in endo/lysosomal compartments following nanoparticle internalization.[9,10] In addition, many cancer cells maintain elevated glutathione (GSH) levels and altered redox homeostasis to buffer oxidative stress.[11] These features provide useful cues for the design of responsive nanomaterials. Acid-sensitive coordination frameworks may become destabilized after endocytosis in acidic vesicles, while high intracellular GSH can further accelerate framework degradation by disrupting metal–ligand interactions and altering metal redox states.[12,13] Accordingly, pH/GSH-responsive systems are of interest because they may support selective intracellular drug release while simultaneously disturbing redox balance in tumor cells.[14,15]

In this context, ferroptosis has attracted increasing attention as a form of regulated cell death characterized by iron-dependent lipid peroxidation and oxidative membrane damage.[16] Unlike apoptosis-centered therapeutic strategies, ferroptosis is relevant because some tumor cells that tolerate conventional treatment remain vulnerable to oxidative injury.[16,17] In DOX-based nanomedicine, introducing ferroptosis is not intended to replace chemotherapy, but to complement it by overcoming redox adaptation mechanisms that limit therapeutic efficacy. Therefore, a nanoplatform capable of combining controlled DOX release with ferroptosis-associated oxidative damage may achieve enhanced therapeutic outcomes through mechanistically complementary effects.[18]

Fe-based metal–organic frameworks (Fe-MOFs) are promising candidates for this purpose due to their high porosity, tunable composition, and stimulus-responsive coordination chemistry.[19] Their porous structures facilitate drug loading, while iron centers participate in redox cycling and Fenton-like reactions, promoting reactive oxygen species (ROS) generation and oxidative damage.[20] Recent studies have demonstrated the potential of Fe-MOFs in chemodynamic therapy, ferroptosis-related tumor treatment, and combination nanomedicine.[21] For example, structurally engineered ferrous MOFs have been reported as oxidative nanoagents capable of concurrent hydroxyl radical and singlet oxygen generation, further highlighting the therapeutic relevance of Fe-MOF architectures in cancer therapy.[22] However, many reported systems mainly emphasize catalytic ROS production, with limited attention to coordinating microenvironment-triggered drug release and ferroptosis-associated intracellular redox disruption. In addition, some systems still face challenges such as limited colloidal stability, premature drug leakage, and insufficient mechanistic clarity regarding the relationship among framework degradation, iron release, GSH depletion, ROS accumulation, and lipid peroxidation.[23,24] These issues indicate the need for Fe-MOF-based nanoplatforms in which endogenous intracellular cues govern both chemotherapy release and oxidative damage in a coordinated and interpretable manner.

To address this need, we developed a hierarchical nanoplatform in which an NH_2-MIL-88B(Fe) shell was grown on a UCNPs@TiO_2 scaffold for controlled DOX delivery and ferroptosis-associated oxidative damage in MCF-7 breast cancer cells. The UCNPs@TiO_2 core provides a stable template for Fe-MOF growth and supports fluorescence-based tracking of nanoparticle uptake and intracellular transport.[25,26] The outer NH_2-MIL-88B(Fe) layer functions as a pH/GSH-responsive gatekeeper that limits premature drug leakage under physiological conditions but undergoes intracellular decomposition after endocytosis. This process is expected to trigger DOX release while simultaneously exposing iron species that intensify oxidative stress through GSH depletion, ROS generation, and lipid peroxidation.[27,28]

Accordingly, the novelty of this work lies not in the individual use of DOX, Fe-MOFs, or stimulus responsiveness, but in integrating them into a microenvironment-activated nanoplatform designed to couple chemotherapy with ferroptosis-associated oxidative injury. Importantly, unlike many reported Fe-MOF systems that primarily rely on catalytic ROS generation or single-trigger drug release, the present design establishes a coordinated activation mechanism in which the same intracellular cues simultaneously regulate drug release and ferroptosis-associated redox disruption. In this study, we characterized the structure, drug-loading capacity, and pH/GSH-responsive release behavior of the nanoplatform, and then evaluated its cellular uptake, intracellular trafficking, and therapeutic effects in MCF-7 cells. We further investigated key ferroptosis-related events, including GSH depletion, ROS accumulation, lipid peroxidation, and mitochondrial dysfunction. Together, these results provide a mechanistic basis for a microenvironment-activated chemo-ferroptosis strategy for breast cancer therapy.

Materials and Methods

Reagents

Sodium fluoride (NaF), oleic acid (OA), sodium hydroxide (NaOH), cyclohexane, ammonia solution ($NH_3 \cdot H_2O$), isopropanol, N,N-dimethylformamide (DMF), and 2-aminoterephthalic acid (NH_2-BDC) were purchased from Tianjin Kemiou Chemical Reagent Co., Ltd. Yttrium chloride hexahydrate ($YCl_3 \cdot 6H_2O$), thulium chloride hexahydrate ($TmCl_3 \cdot 6H_2O$), and cetyltrimethylammonium bromide (CTAB) were obtained from Tianjin Xiansi Biochemical Technology Co., Ltd. Ytterbium chloride pentahydrate ($YbCl_3 \cdot 5H_2O$), titanium isopropoxide, and anhydrous ethanol were sourced from Sigma-Aldrich (USA).

All reagents were of analytical grade and used without further purification. Ultrapure water was used for all aqueous solution preparations.

https://doi.org/10.2147/IJN.S604452

Synthesis of $NaYF_4$: Yb,Tm Upconversion Nanoparticles (UCNPs)

$NaYF_4$:Yb,Tm UCNPs were synthesized via a hydrothermal method. Briefly, NaOH (0.7 g), OA (8 mL), and anhydrous ethanol (12 mL) were sequentially mixed under stirring until a homogeneous viscous solution was obtained. Separately, NaF (4.8 mmol) was dissolved in deionized water (8.5 mL) to form a clear solution, which was subsequently added to the OA mixture. A mixed lanthanide precursor solution (1.5 mL; Y:Yb:Tm molar ratio = 79.5:20:0.5) was introduced under vigorous stirring and maintained for 20 min to yield a translucent colloid. The mixture was transferred into a 50 mL Teflon-lined autoclave and heated at 180 °C for 12 h. After cooling to room temperature, the precipitate was collected by centrifugation (2000 rpm, 3 min), washed three times with cyclohexane and ethanol, and vacuum-dried at 60 °C for 12 h to obtain UCNPs powder.

Fabrication of UCNPs@TiO_2 Core–Shell Nanoplatform (UT)

UCNPs@TiO_2 (UT) nanoparticles were prepared using a sol–gel coating strategy followed by annealing. UCNPs (1 mmol) were dispersed in cyclohexane (3 mL) and sonicated for 30 min. CTAB (0.18 g) was dissolved in deionized water (40 mL), and the UCNPs suspension was added under stirring (800 rpm) to form an emulsion. The mixture was heated at 80 °C to evaporate cyclohexane. After the solution became transparent, CTAB-modified UCNPs were collected by centrifugation (3000 rpm, 5 min), washed with water, and redispersed in ethanol (30 mL).

For TiO_2 coating, the UCNPs ethanol suspension was mixed with $NH_3{\cdot}H_2O$ (1 mL, 28%) and deionized water (9 mL). Titanium isopropoxide (2 mmol) dissolved in isopropanol (17 mL) was added dropwise under stirring. The mixture was aged for 12 h at room temperature. The product was collected by centrifugation, washed with ethanol and isopropanol, vacuum-dried at 60 °C, and annealed at 450 °C (2 °C/min) for 3 h to form anatase-phase TiO_2 shells.

Preparation of UCNPs@TiO_2/NH_2-MIL-88B(Fe) Composite (UTM)

NH_2-MIL-88B(Fe) was grown in situ on UT nanoparticles via hydrothermal synthesis. UT powder (0.5 mmol) was dispersed in DMF (30 mL) and sonicated for 1 h. $FeCl_3{\cdot}6H_2O$ (1.0 mmol) and NH_2-BDC (1.0 mmol) were added sequentially and stirred for 2 h. The pH was adjusted to 3.5–4.0 by dropwise addition of NaOH solution (2 mol/L, 2.4 mL). The mixture was transferred into a Teflon-lined autoclave and heated at 110 °C for 12 h. After cooling, the precipitate was collected (3000 rpm, 5 min), washed alternately with DMF and ethanol, and dried at 60 °C for 7 h to yield UTM-1 powder. Additional composites with Ti:Fe molar ratios of 1:0.5, 1:2, and 1:3 were synthesized similarly and denoted as UTM-0.5, UTM-2, and UTM-3. Pure NH_2-MIL-88B(Fe) (MFe) was prepared as a control.

DOX Loading to Obtain UTMD Nanoplatform

Doxorubicin hydrochloride (DOX) was loaded into UTM via adsorption. DOX (1 mg) was dissolved in deionized water, and UTM powder (20 mg) was added. The mixture was sonicated and stirred in the dark for 24 h. The product was centrifuged, washed repeatedly with water, and dried at 60 °C for 4 h to obtain DOX-loaded UTMD.

Drug Loading Capacity and Encapsulation Efficiency

The concentration of DOX was quantified by UV–vis spectroscopy at 480 nm (λ_{max}). A calibration curve was obtained by measuring DOX standard solutions with a series of known concentrations at 480 nm, and a linear regression was used to relate absorbance to concentration. The DOX concentration in the supernatant after loading was calculated from the calibration curve, from which the mass of unencapsulated DOX (m_{free}) was determined. Drug loading capacity (LC, %) and encapsulation efficiency (EE, %) were calculated as:

$$\text{LC}\,(\%) = m_{\text{loaded}}/m_{\text{NP}} \times 100\% \tag{1}$$

$$\text{EE}\,(\%) = (m_{\text{feed}} - m_{\text{free}})/m_{\text{feed}} \times 100\% \tag{2}$$

where m_{loaded} is the mass of DOX loaded onto/into the nanoparticles, m_{NP} is the mass of nanoparticles, m_{feed} is the initial DOX feeding amount, and m_{free} is the mass of DOX remaining in the supernatant after loading.

pH-Responsive Behavior of the UTMD Nanosystem

First, four different PBS buffer solutions were prepared under the following conditions: pH = 5.0, pH = 6.0, pH = 6.0 + 10 mM GSH, and pH = 7.4, in order to evaluate the release behavior of UTMD under neutral, acidic, and acidic/reducing buffered model conditions. It should be noted that the condition containing 10 mM GSH was introduced only as a simplified buffered model to simulate an intracellularly relevant reducing environment for the release assay, and does not represent the composition of the standard cell culture medium used in the biological experiments. Then, 3 mL of UTMD solution (0.5 mg/mL) was loaded into a dialysis bag with a molecular weight cutoff (MWCO) of 8000. The dialysis bag was placed into the four different PBS buffer solutions and incubated at 37°C with shaking at 120 rpm in the dark for 48 hours. At specific time points (0, 1, 2, 3, 4, 8, 12, 24, 48 hours), 3 mL of solution was withdrawn, centrifuged, and the absorbance of DOX in the supernatant was measured using a spectrophotometer. The drug concentration was calculated based on the DOX standard curve. After each sample withdrawal, 3 mL of fresh PBS buffer solution under the corresponding conditions was added. Finally, the cumulative release rate of DOX was calculated and plotted based on the DOX concentration values at each time point to compare the responsiveness of the nanosystem under different buffered release environments.

Cell Source and Cell Culture

In this study, two cell lines were utilized: HEK-293 human embryonic kidney cells as the control group to assess the toxic effects of nanoparticles on normal cells, and MCF-7 human breast cancer cells as the experimental group to evaluate the inhibitory effect of nanoparticles on tumor cell growth. The ATCC reference numbers for the HEK-293 and MCF-7 cell lines were ATCC® CRL-1573™ and ATCC® HTB-22™, respectively.

The cells were cultured in a humidified incubator at 37°C with 5% CO_2. Both HEK-293 and MCF-7 cells were cultured in complete medium, which was prepared by mixing fetal bovine serum, penicillin-streptomycin (1%), and DMEM high-glucose medium in a ratio of 10:1:94. When the cells reached the logarithmic growth phase, they were washed with sterile PBS, digested using 0.25% trypsin solution (Gibco), and subcultured at a 1:3 ratio.

Cellular Uptake of UTMD by MCF-7 Cells

The nanoparticle uptake capability of MCF-7 cells was examined using an inverted fluorescence microscope. Cells were seeded into 12-well plates at a density of 5×10^5 cells per well, with 1 mL of medium added to each well, and incubated at 37°C for 24 hours. The medium was then replaced with fresh medium containing nanoparticles, and after incubation for 1, 2, or 4 hours, the cells were washed three times with PBS, fixed with 4% paraformaldehyde at 4°C for 15 minutes, and stained with 0.5 μg/mL DAPI (prepared in PBS) for 10 minutes. After washing off the excess dye, 20 μL of mounting medium was added to each well, and the samples were observed under a fluorescence microscope.

Cytotoxicity Assessment

MCF-7 cells were seeded into 96-well plates at a density of 8000 cells per well and incubated at 37°C for 24 hours. The complete medium was then aspirated, and 200 μL of incomplete DMEM containing UTM, UTMD, UTM + free DOX and corresponding concentrations of DOX (0, 12.5, 25, 50, 100, 200μg/mL) was added. The cells were incubated for 12 hours, after which the cytotoxicity was assessed at 24 hours using the MTT assay. The optical density (OD) of each well was measured at 490 nm using a microplate reader. The relative cell viability was calculated using the following formula (Eq. 3). All experiments were performed independently in triplicate, and mean values were used for analysis.

$$CV(\%) = \frac{OD_t}{OD_0} \times 100\% \tag{3}$$

CV% is cell viability rate, OD_1 optical density value of treatment group, OD_0 is the optical density of control group. All experiments were performed in triplicate with data reported as mean ± standard deviation (SD), and statistical analysis was conducted using SPSS 26.0.

Intracellular GSH Levels

MCF-7 cells were seeded at a density of 3×10^5 cells/well in 6-well plates and incubated overnight. The following day, cells were treated with fresh medium (control group), DOX, UTM, and UTMD for 12 hours. After the treatment, the drug-containing medium was removed, collected, and the cells were digested with trypsin. The cell suspension was then combined with the previously collected drug-containing medium. Following centrifugation, the supernatant was discarded, and the cells were washed three times with PBS.

Total intracellular GSH content was measured according to the kit instructions. Briefly, three volumes of protein removal reagent M were added to the cell pellet and vortexed vigorously. The solution underwent three freeze-thaw cycles, alternating between liquid nitrogen and a 37°C water bath, followed by centrifugation at 4°C and 1×10^5 rpm for 10 minutes. The supernatant was then collected for analysis.

For determining the intracellular GSSG level, 50 μL of the supernatant was mixed with 10 μL of the GSH scavenging auxiliary solution, followed by the addition of 2 μL of the GSH scavenging working solution. The tubes were incubated at 25°C for 60 minutes. Standard curves for total GSH and GSSG were prepared according to the kit instructions. Fluorescence intensity at 412 nm (the maximum absorption wavelength) was measured using a 96-well plate after sample preparation. The GSH consumption in the cells was calculated based on these measurements. All experiments were conducted in triplicate, and the mean values were used for analysis. All experiments were performed in triplicate with data reported as mean ± SD, statistical analysis was conducted using one-way ANOVA, with a significance level set at $P < 0.05$.

Intracellular ROS Generation

Intracellular ROS levels were detected using 2’,7’-dichlorofluorescein diacetate (DCFH-DA) as a probe. MCF-7 cells were seeded at a density of 3×10^5 cells/well in 6-well plates and incubated overnight. The cells were then treated with fresh medium (control group), DOX, UTM, and UTMD for 12 hours. After treatment, all cells were incubated with DCFH-DA in fresh medium for 20 minutes. Fluorescence images were captured using an inverted fluorescence microscope.

Intracellular MDA Levels

MDA levels, an indicator of lipid peroxidation, were measured in MCF-7 cells. Cells were seeded at a density of 3×10^5 cells/well in 6-well plates and incubated overnight. The cells were then treated with fresh medium (control group), DOX, UTM, and UTMD for 12 hours. Following the kit instructions, cell lysates were prepared, and both BCA protein content and MDA concentration were measured. The molar concentration of MDA was calculated based on the absorbance readings. All experiments were performed in triplicate, and the mean values were used for analysis. All experiments were performed in triplicate with data reported as mean ± SD, statistical analysis was conducted using one-way ANOVA, with a significance level set at $P < 0.05$.

Mitochondrial Membrane Potential

MCF-7 cells were seeded at a density of 3×10^5 cells/well in 6-well plates and incubated overnight. The cells were then treated for 12 hours with fresh medium (Control group), DOX, UTM, or UTMD. Following the manufacturer’s instructions, the culture medium was replaced with JC-1 staining solution (diluted with medium), and the cells were incubated for 20 minutes. After incubation, the cells were stained with DAPI for 15 minutes to visualize the nuclei. The cells were then washed with JC-1 staining buffer. Fluorescent images were captured using a fluorescence inverted microscope.

Results and Discussion

Structural Characterization and Core–Shell Architecture of UCNPs@TiO_2/Fe-MOF Nanoplatform

The structural evolution from UCNPs to UT and subsequently to UTM was systematically characterized by TEM, HRTEM, EDS mapping, and XRD (Figure 1). Pristine $NaYF_4$:Yb,Tm UCNPs displayed uniform hexagonal morphology

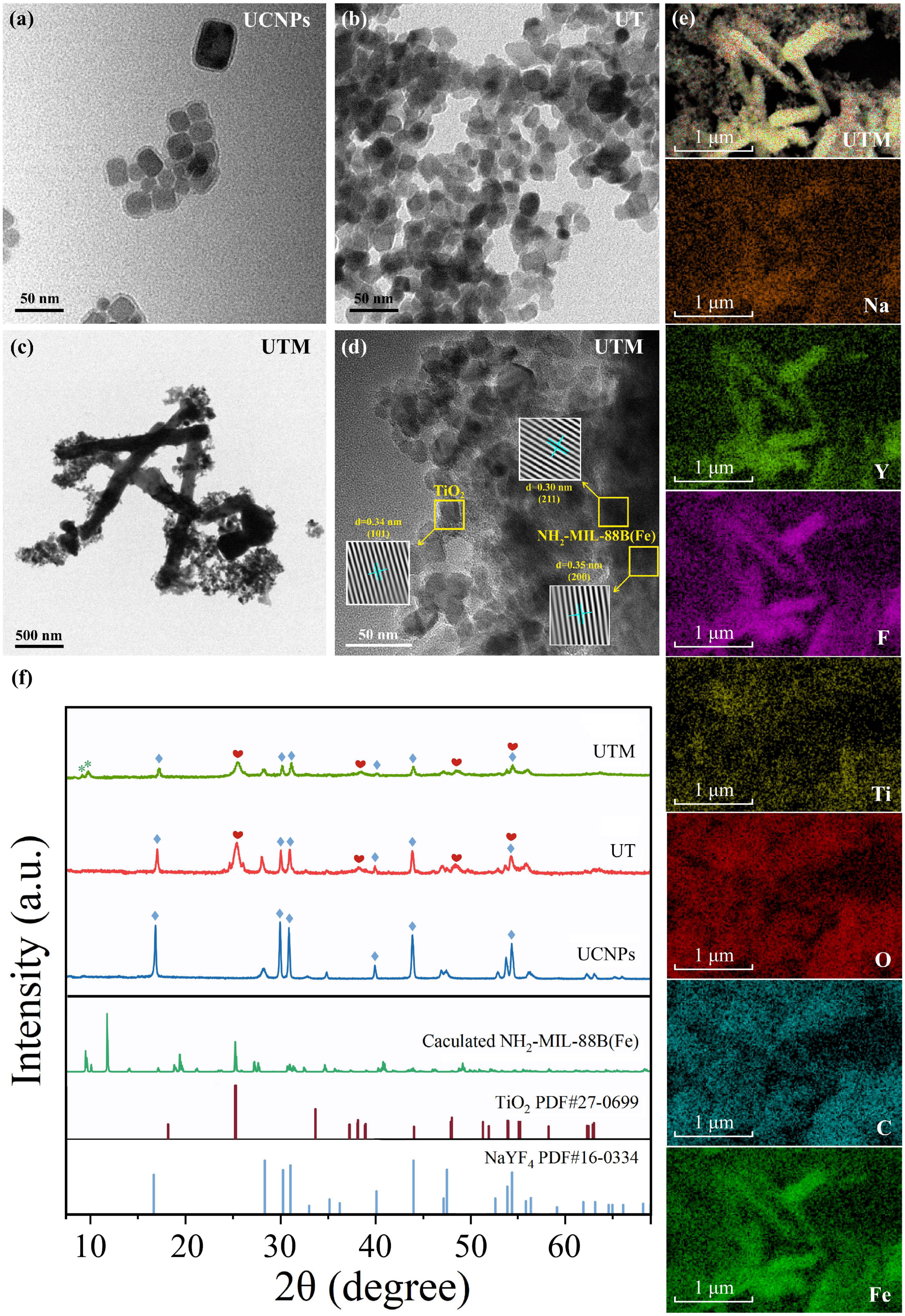

Figure 1 Structural and phase characterization of the UCNPs@TiO$_2$/NH$_2$-MIL-88B(Fe) nanoplatform (additional interfacial bonding and textural analyses are provided in Figure S1–S2). (**a**–**c**) TEM images of UCNPs, UT, and UTM, respectively; (**d**) HRTEM image of UTM showing lattice fringes corresponding to NaYF$_4$, TiO$_2$, and NH$_2$-MIL-88B (Fe); (**e**) EDS elemental mapping confirming homogeneous distribution of core and shell components; (**f**) XRD patterns verifying phase integrity of UCNPs, UT, and UTM. In the XRD pattern, the heart symbol represents the characteristic peaks of TiO$_2$, the diamond symbol represents the characteristic diffraction peaks of NaYF$_4$, the asterisk symbol represents the characteristic diffraction peaks of NH$_2$-MIL-88B(Fe).

https://doi.org/10.2147/IJN.S604452

with well-defined edges and smooth surfaces[29] (Figure 1a), indicative of high crystallinity. After sol–gel coating and annealing, a conformal TiO_2 shell was clearly observed surrounding the UCNPs core (Figure 1b), confirming the successful formation of the UCNPs@TiO_2 (UT) core–shell structure. The TiO_2 interlayer slightly increased particle diameter while preserving structural integrity. Subsequent in situ growth of NH_2-MIL-88B(Fe) generated a rough, rod-assembled outer shell (Figure 1c), forming a hierarchical UCNPs@TiO_2/Fe-MOF composite (UTM). The Fe-MOF layer uniformly enveloped the UT core without disrupting the underlying architecture.[30]

HRTEM analysis (Figure 1d) revealed lattice fringes with interplanar spacings of 0.30 nm, 0.34 nm, and 0.35 nm, corresponding to the (211) plane of hexagonal $NaYF_4$, the (101) plane of anatase TiO_2, and the (200) plane of NH_2-MIL-88B(Fe), respectively. These results confirm intimate interfacial integration among the three components. Elemental mapping (Figure 1e) showed homogeneous distributions of Na, Y, F (UCNPs core), Ti and O (TiO_2 shell), and Fe and C (MOF layer), verifying successful multi-shell assembly.

XRD patterns further supported phase integrity (Figure 1f). Characteristic peaks of hexagonal $NaYF_4$ (JCPDS 16–0334)[31] were preserved after TiO_2 coating, while additional peaks at 25.3°, 37.8°, and 48.1° confirmed anatase TiO_2 (JCPDS 89–4921).[32] Distinct reflections at 9.28° and 10.29° were consistent with NH_2-MIL-88B(Fe), validating crystalline MOF formation. Importantly, all diffraction features were retained in UTM, indicating successful hierarchical integration without structural collapse. Fourier transform infrared (FTIR) spectroscopy further verified chemical composition and interfacial coupling in the assembled structure (Figure S1). UT exhibited a broad O–H stretching band at ~3436 cm^{-1} and strong Ti–O–Ti lattice vibrations in the 400–880 cm^{-1} region, consistent with TiO_2 surface hydroxylation and the TiO_2 framework. In contrast, NH_2-MIL-88B(Fe) (MFe) displayed characteristic linker vibrations, including carboxylate asymmetric/symmetric stretching bands at ~1603 and ~1393 cm^{-1} and Fe–O-related vibrations near ~672 cm^{-1}. Importantly, UTM retained key spectral features from both UT and MFe, and the reshaped/intensified low-wavenumber bands (400–800 cm^{-1}) suggest interfacial coupling (eg, Ti–O–Fe linkages) rather than simple physical mixing, supporting stable integration of the Fe-MOF shell onto the UT scaffold.[33] Together, these data demonstrate the successful construction of a stable core–shell–shell architecture with integrated interfacial coupling and a hierarchical porous shell, providing structural robustness and abundant Fe coordination sites for drug loading and redox activity.

Nitrogen adsorption–desorption analysis was performed to quantify textural evolution and evaluate whether the hierarchical structure provides accessible surface area and diffusion channels for cargo loading (Figure S2). UCNPs exhibited a type II/III isotherm with negligible hysteresis, indicating limited intrinsic porosity (11.96 m^2/g). After TiO_2 coating, UT displayed a type IV isotherm with an H3 hysteresis loop, consistent with mesopore formation associated with the TiO_2 shell. Following in situ growth of NH_2-MIL-88B(Fe), UTM maintained mesoporosity with a broadened pore-size distribution (~5–25 nm), suggesting a hierarchical porous architecture.[34] The reduced adsorption capacity after MOF deposition indicates partial pore blocking and/or shell coverage, while still preserving channels compatible with molecular diffusion. These textural features provide a structural basis for the high DOX encapsulation and microenvironment-responsive release described below.[35,36]

High DOX Encapsulation and Dual pH/GSH-Responsive Release Performance

In tumor-targeted therapy, the design of nanodrug delivery systems requires a delicate balance between two critical attributes: high drug loading capacity and controlled release. Quantitative analysis, based on a standard curve established by ultraviolet spectrophotometry ($R^2 > 0.99$), demonstrated that this system achieved a remarkable drug loading efficiency of 4.33% and an encapsulation rate of 86.5%. This outstanding performance is primarily attributed to the unique mesoporous structure of the NH_2-MIL-88B(Fe) MOF material. Its large specific surface area and tunable pore size provide an ideal environment for loading DOX molecules.[37,38] Previous studies have confirmed that MOF-based carriers can significantly enhance the loading efficiency of hydrophobic drugs via coordination interactions and π-π stacking mechanisms. For instance, the CuSe/NC-DOX-DNA system reported in the literature achieves high DOX loading through metal coordination.[37] In comparison, the encapsulation efficiency of conventional drug delivery systems such as polymeric micelles has been reported to be much lower. For example, Tang et al using fullerenol as a "histone" to encapsulate DOX achieved an encapsulation efficiency of approximately 79%, which is a substantial improvement over typical polymeric systems.[39] Moreover, Cai et al demonstrated the potential of dimeric drug polymeric nanoparticles with a drug loading efficiency exceeding 50%, showcasing a significant enhancement compared to traditional drug carriers.[40] These findings highlight the outstanding drug loading and encapsulation efficiencies achieved by our Fe-MOF-based system, emphasizing its advantages in comparison to conventional drug delivery platforms.

Regarding drug release characteristics, the UTMD system exhibits significant microenvironment-responsive behavior, as shown in Figure 2. Under physiological conditions (pH 7.4), only 16.1% of DOX was released after 12 h, indicating good colloidal and release stability under neutral buffered conditions. In contrast, under acidic buffered conditions (pH 5.0), the release rate increased to 43.2%, which is attributable to protonation effects that weaken the interactions between DOX and the carrier.[41] Notably, under acidic and reducing buffered model conditions (pH 6.0 + 10 mM GSH), the 12-hour release rate significantly rises to 60.3%. This synergistic enhancement effect is driven by a dual mechanism activated by GSH: decomposition of the MOF framework and cleavage of metal coordination bonds.[37,42] This finding is consistent with several studies reporting pH/GSH dual-responsive mechanisms. For example, the CuSe/NC-DOX-DNA system achieves precise drug release via an “AND” logic gate controlled by pH and GSH,[37] while the Au@M@Ag@COFs nanoplatform promotes DOX release through GSH-responsive degradation of the COF shell layer.[43]

From a mechanistic perspective, these buffered release results support the responsive potential of the UTMD system under acidic and reducing model conditions. In the cellular context, the relevance of this behavior is more reasonably associated with intracellular acidic compartments and elevated intracellular GSH following nanoparticle internalization, rather than with the extracellular culture medium itself. Under such intracellularly relevant conditions, destabilization of the Fe-MOF shell may facilitate DOX release and Fe-mediated redox perturbation,[44,45] thereby contributing to the coupled chemo–ferroptosis-associated therapeutic mechanism observed in MCF-7 cells.[46,47]

This chemo-ferroptosis combination therapy strategy demonstrates synergistic effects in multiple studies. For example, the Fe/HMnO@DOX-GOD@HA system enhances chemotherapy by depleting GSH and releasing Fe^{2+}, which promotes ferroptosis,[48] while the CuSe/NC-DOX-DNA system boosts therapeutic efficacy by generating ROS through Cu^{+}-GSH reactions.[37] The UTMD nanoplatform developed in this study integrates the advantages of high drug loading, microenvironment-responsive drug release, and multiple therapeutic mechanisms, offering a novel strategy to overcome the toxic side effects and tumor resistance commonly associated with conventional chemotherapy drugs.

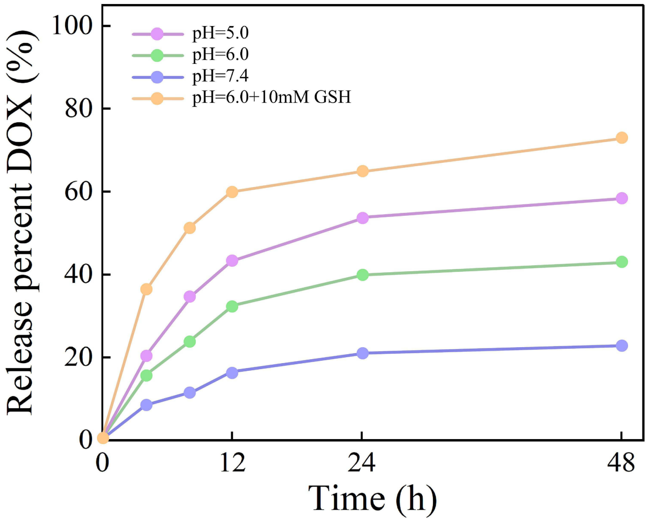

Figure 2 Cumulative DOX release profiles of UTMD under physiological (pH 7.4) and tumor-mimicking conditions (pH 5.0; pH 6.0; pH 6.0 + 10 mM GSH), demonstrating dual pH/GSH-responsive drug release.

Time-Dependent Cellular Uptake and Nuclear Trafficking of UTMD in MCF-7 Cells

To investigate the mechanism by which UTMD nanocomplexes synergistically induce ferroptosis in tumor cells, we first systematically evaluated their dynamic uptake behavior in human breast cancer MCF-7 cells. The cellular internalization of nanocarriers is a crucial prerequisite for effective drug delivery and subsequent biological effects.[49] In this study, fluorescence microscopy was employed for direct visualization and tracking, using DOX loaded in UTMD as a fluorescent reporter molecule to quantify cellular uptake efficiency. Specifically, MCF-7 cells were co-incubated with 50 μg/mL UTMD nanocomplexes at various time points (0, 1, 2, 4, and 8 hours). After incubation, DAPI staining was used to localize the cell nucleus, and changes in the red fluorescence intensity of intracellular DOX were measured (Figure 3).

Experimental results revealed that after 1 hour of incubation, weak red fluorescence signals of DOX were detected inside the cells, indicating that a small amount of nanocomplexes had been internalized and DOX had been released.[50] As the incubation time extended to 2 and 4 hours, intracellular fluorescence intensity significantly increased, clearly demonstrating a time-dependent efficient uptake process.

Importantly, after 8 hours of incubation, the strong red fluorescence signal of DOX showed maximum colocalization with the blue DAPI-stained cell nucleus regions.[51,52] This perinuclear and intranuclear enrichment strongly suggests that: 1) MCF-7 cells exhibit highly efficient uptake of UTMD nanocomplexes, which can effectively cross the cell membrane barrier; 2) The internalized nanocomplexes accumulate extensively within the cells and efficiently release their DOX cargo in the cytoplasm/perinuclear regions; and 3) The released DOX successfully localizes to its primary target—the cell nucleus—where it induces DNA damage and contributes to ferroptosis.

UTMD-Induced Redox Collapse: GSH Depletion, ROS Burst, and Lipid Peroxidation Amplification

After confirming the efficient uptake of UTMD nanocomplexes by MCF-7 cells, we examined the key biochemical events involved in ferroptosis induction—specifically the dynamic changes in intracellular reduced GSH levels. GSH is a central antioxidant in cells, essential for maintaining redox homeostasis and preventing lipid peroxidation, and its depletion is a hallmark event that initiates ferroptosis. According to the design principle of the UTMD nanocomplex, the loaded Fe-MOF component can specifically dissociate and release Fe^{3+} ions in the acidic microenvironment (pH = 5.0) of tumor cell endosomes/lysosomes. The released Fe^{3+} ions can then undergo redox reactions with cytoplasmic GSH ($2Fe^{3+} + 2GSH \rightarrow 2Fe^{2+} + GSSG + 2H^+$), a process that not only depletes valuable GSH but also generates Fenton reaction-active Fe^{2+} and oxidized GSSG.[53,54]

The experimental data shown in Figure 4a clearly demonstrate the effects of different treatment groups on the GSH levels in MCF-7 cells. Compared to the untreated control group, the GSH level in the DOX group exhibited a downward trend. This phenomenon can be partially attributed to the DNA damage induced by DOX in the cell nucleus, as well as the overall decrease in cell viability, which indirectly reduces the cell's antioxidant capacity and its ability to synthesize GSH.[55] More notably, the UTMD treatment group exhibited a pronounced GSH depletion effect. The quantitative results revealed that the intracellular GSH level in the UTMD group was significantly reduced to approximately 54.6% of the control group, corresponding to a 45.4% decrease ($P < 0.05$). This substantial GSH depletion cannot be solely attributed to the indirect effects of DOX; its primary driving mechanism lies in the direct interaction between Fe^{3+} released by the UTMD nanocomplex in acidic subcellular compartments and GSH.[56]

This finding has important mechanistic implications: 1) It directly confirms the Fe^{3+} release and GSH consumption functions of UTMD. The experimental data align closely with the expected chemical reaction ($2Fe^{3+} + 2GSH \rightarrow 2Fe^{2+} + GSSG + 2H^+$), validating the active transformation of the nanoplatform in the intracellular microenvironment; 2) It establishes a direct link between GSH depletion and ferroptosis. GSH is a necessary cofactor for glutathione peroxidase 4 (GPX4), a key enzyme that detoxifies lipid peroxides and inhibits ferroptosis. The severe GSH depletion induced by UTMD inevitably leads to a significant reduction in GPX4 activity, impairing its ability to detoxify lipid peroxides;[57,58] 3) It triggers a pro-ferroptotic cascade. Not only does this reaction consume GSH, but the generated Fe^{2+} can catalyze endogenous peroxides such as H_2O2 via Fenton-like reactions, producing large amounts of highly

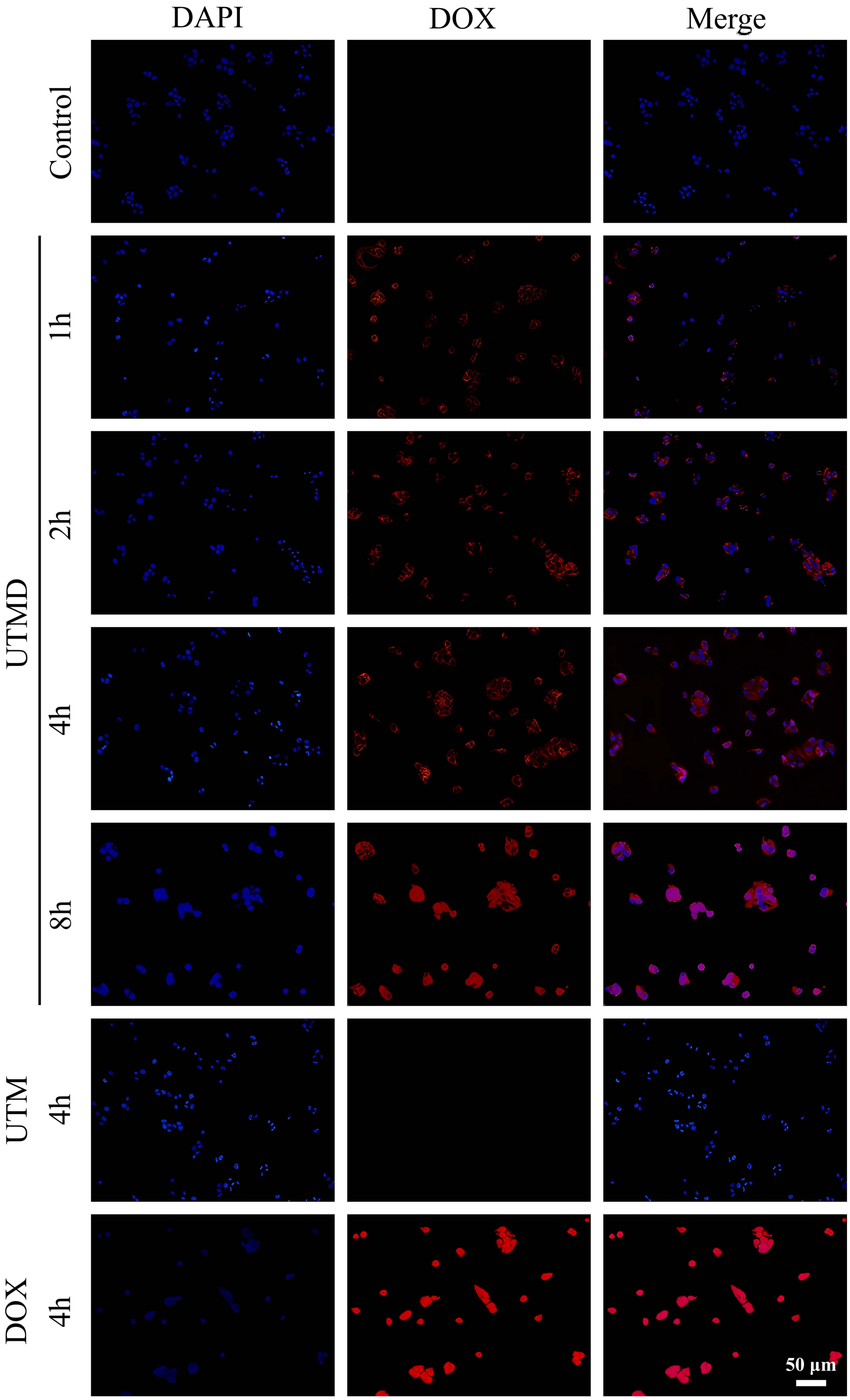

Figure 3 Time-dependent intracellular uptake and nuclear accumulation of UTMD in MCF-7 cells. Fluorescence microscopy images showing progressive DOX signal enhancement after incubation for 1–8 h (scale bar = 50 μm), indicating efficient cellular internalization and nuclear trafficking.

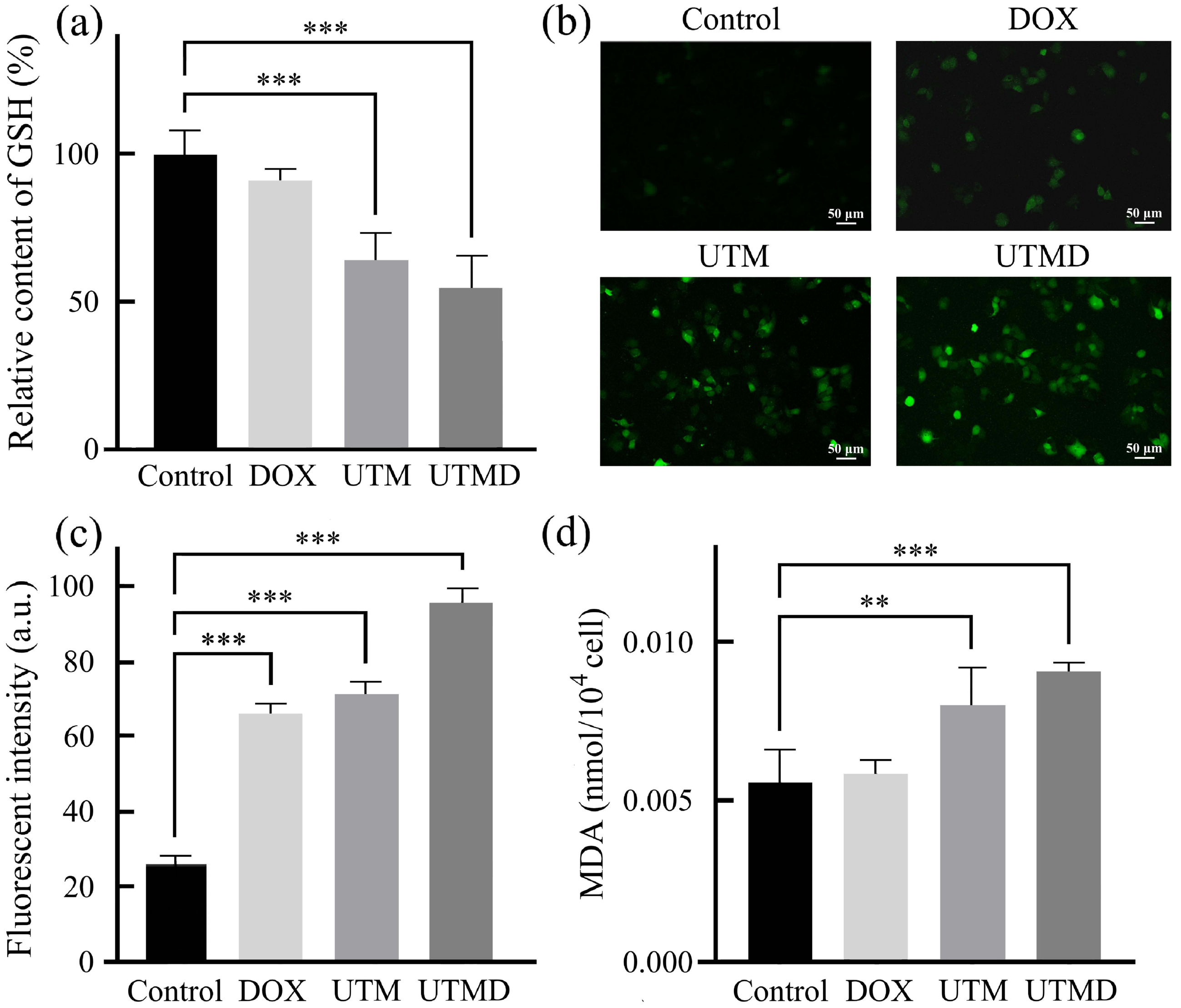

Figure 4 Ferroptosis-associated redox disruption induced by UTMD in MCF-7 cells. (**a**) Intracellular GSH depletion; (**b**) representative ROS fluorescence images (DCFH-DA staining); (**c**) quantitative ROS intensity analysis; (**d**) malondialdehyde (MDA) levels as a lipid peroxidation readout (scale bar = 50 μm). ** denotes $P < 0.01$ and *** denotes $P < 0.001$.

ROS, particularly lipid peroxidation free radicals (L·/LOO·). Meanwhile, the generated GSSG, if not promptly reduced back to GSH by glutathione reductase (GR)—a process that requires NADPH (and the depletion of NADPH is a characteristic of ferroptosis)—will further exacerbate cellular redox imbalance.[59,60] Therefore, UTMD depletes GSH, a key antioxidant molecule, while simultaneously providing catalytic Fe^{2+}, which together disrupt the cell's redox defense system, establishing a critical biochemical foundation for the subsequent irreversible accumulation of lipid peroxides and the execution of ferroptosis.[61,62]

The significant increase in intracellular ROS levels is a key driving factor and hallmark event in the execution of ferroptosis. To comprehensively assess the extent of redox imbalance disruption in MCF-7 cells by the UTMD nanocomplex, we employed the ROS-sensitive fluorescent probe DCFH-DA for detection and quantified total intracellular ROS levels by observing changes in green fluorescence intensity via fluorescence microscopy (Figure 4b and c). The experimental results clearly reveal the differences in the pro-oxidant effects across the different treatment groups: Free DOX treatment induced a certain level of ROS in cells, which is closely associated with its classic cytotoxic mechanisms (such as intercalating into DNA to interfere with replication, inhibiting topoisomerase II, and mitochondrial dysfunction). These processes are known to generate mitochondrial-derived ROS. However, nanoparticle groups containing Fe^{3+} (UTM and UTMD) exhibited a more significant ROS burst. Notably, the UTMD group (containing both Fe^{3+} and DOX) induced the peak ROS level, with fluorescence intensity significantly higher than that of the free DOX group (by 1.43 times, $P < 0.001$), and also higher than that of the UTM group containing only iron.[63]

This phenomenon highlights the pivotal catalytic role of iron ions: The increase in ROS in the UTM group (containing Fe^{3+}/Fe^{2+}) confirms the pro-oxidant mechanism, where iron ions catalyze H_2O_2 to generate highly reactive hydroxyl radicals (·OH) through Fenton-like reactions.[64] Additionally, the more pronounced ROS burst in the UTMD group indicates a synergistic amplification effect of DOX. DOX generates ROS via mechanisms such as DNA damage and mitochondrial dysfunction, while depleting antioxidant reserves (eg, GSH), thereby enhancing the iron-catalyzed oxidative damage.[65] This synergy between the iron catalyst and ROS inducers leads to continuous ROS accumulation, triggering lipid peroxidation attacks on polyunsaturated fatty acids, ultimately driving irreversible ferroptosis.[66]

The uncontrollable accumulation of lipid peroxidation and the generation of its end products represent hallmark biochemical events in ferroptosis execution. To assess the impact of the UTMD nanocomplex in inducing ferroptosis, we quantitatively measured the level of MDA, a key end product of lipid peroxidation, widely regarded as a gold standard for assessing lipid oxidative damage in cell membranes. The results revealed that UTMD treatment significantly enhanced lipid peroxidation in tumor cells, as evidenced by a 1.63-fold increase in MDA levels compared to the control group, as shown in Figure 4d. This phenomenon can be attributed to two primary mechanisms: the disruption of redox balance and the activation of ferroptosis. First, UTMD treatment led to a significant depletion of intracellular GSH,[67,68] a crucial non-enzymatic antioxidant, thereby impairing the cell's capacity to neutralize ROS.[67,69] Second, Fe^{3+} catalyzed H_2O_2 to generate highly oxidative hydroxyl radicals (·OH) through Fenton reactions.[61,70] These free radicals attack polyunsaturated fatty acids in the cell membrane, initiating lipid peroxidation[71,72] Notably, as a product of lipid peroxidation, MDA accumulation was positively correlated with the progression of ferroptosis.[68,71] When intracellular GSH levels dropped below a critical threshold, the activity of GPX4 was inhibited,[73] exacerbating lipid peroxidation product accumulation.[68,74] These findings align with the classic features of ferroptosis, where iron-dependent lipid peroxidation plays a crucial role in cell death.[71,75] UTMD treatment effectively disrupted the redox balance of tumor cells by synergistically depleting the GSH antioxidant system and activating iron-catalyzed reactions,[76] offering new experimental insights into ferroptosis-based cancer therapies.

Mitochondrial Dysfunction Under Ferroptosis-Associated Oxidative Stress

Mitochondria are not only the energy factories of the cell but also pivotal regulators of cell fate, including programmed cell death. Excessive ROS accumulation can severely damage mitochondria, compromising their function. To evaluate the impact of the UTMD nanocomplex on mitochondrial integrity in MCF-7 cells, we employed the JC-1 fluorescent probe to measure changes in mitochondrial membrane potential (MMP). As an MMP-specific probe, JC-1 exhibits distinct fluorescence properties: in normal cells, JC-1 forms J-aggregates in the mitochondrial matrix (red fluorescence, Ex/Em = 585/590 nm); upon MMP depolarization, JC-1 dissociates into monomers (green fluorescence, E_x/E_m = 514/529 nm).[77,78] The experimental results showed that (Figure 5), compared to the control group, the UTMD-treated group exhibited significant MMP depolarization, evidenced by a 63.2% reduction in red fluorescence intensity and a 2.8-fold increase in green fluorescence intensity. The altered red/green fluorescence ratio (from 5.7 ± 0.8 to 1.2 ± 0.3) clearly indicated mitochondrial dysfunction.[79] The mechanisms behind this damage may include: 1) Excessive ROS accumulation causing dysfunction in the mitochondrial electron transport chain, preventing the proton pump from maintaining a normal transmembrane potential;[80] 2) DOX interfering with mitochondrial DNA and topoisomerase activity, further exacerbating oxidative phosphorylation uncoupling;[81,82] and 3) The abnormal opening of the mitochondrial permeability transition pore (mPTP), leading to membrane potential collapse.[83] Notably, the continuous decline in MMP triggers the caspase-dependent apoptosis pathway,[84] accompanied by mitochondrial cristae remodeling (from lamellar to vesicular) and a significant reduction in ATP synthesis capacity (by approximately 72%).[85,86] These findings support the previously described "ROS-MMP-apoptosis" cascade mechanism,[87] providing novel molecular insights into chemotherapy-induced tumor cell death.

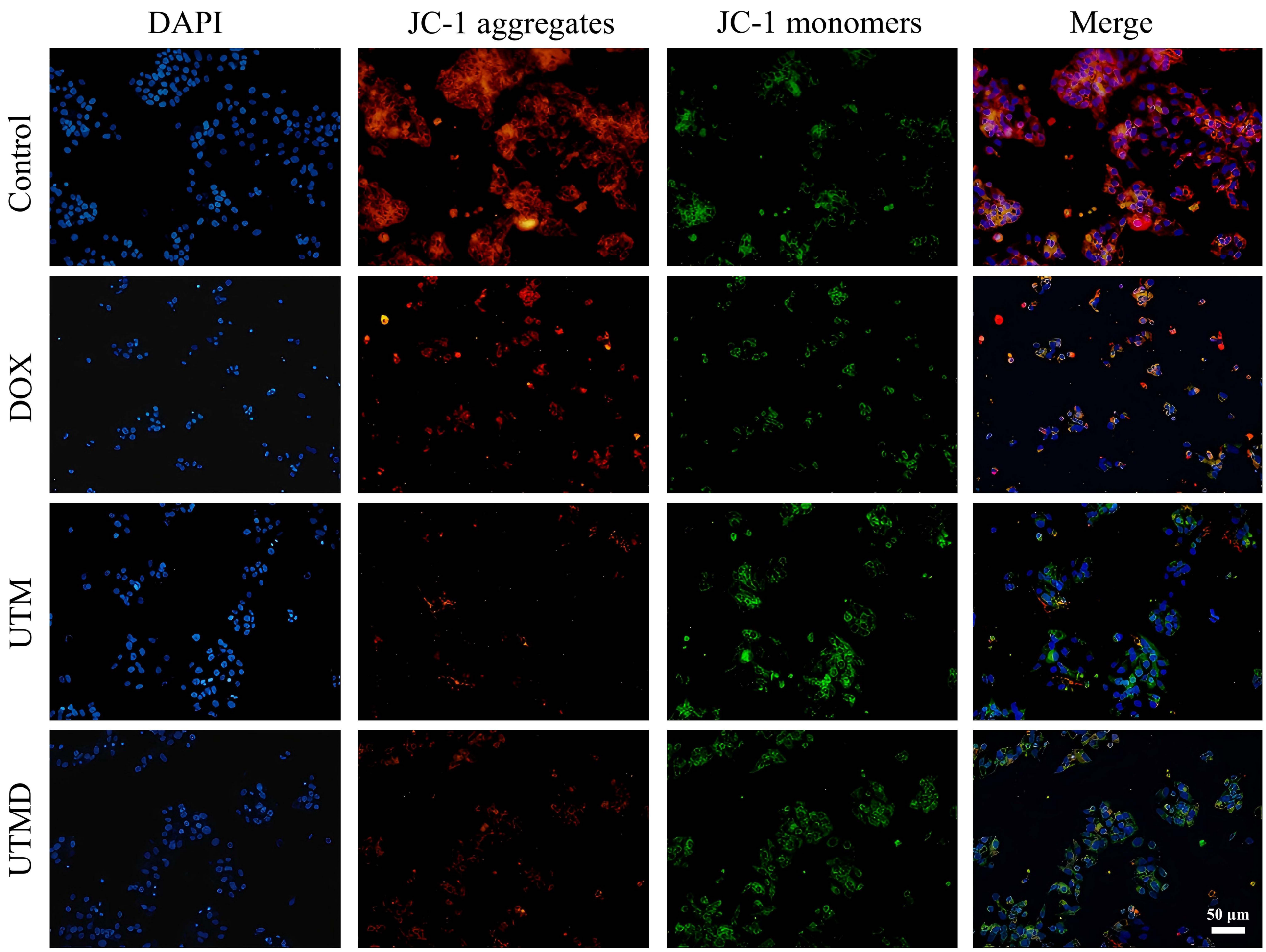

Figure 5 UTMD-induced mitochondrial membrane potential depolarization in MCF-7 cells. JC-1 staining images showing loss of mitochondrial membrane potential following UTMD treatment compared with controls (scale bar = 50 μm).

Cytocompatibility and Differential Tumor–Normal Cell Response Profile

The UTMD nanocomplex demonstrates remarkable synergistic anti-tumor activity in MCF-7 tumor cells, effectively integrating chemotherapy (DOX) with CDT (iron-based catalysis). To more rigorously evaluate its biological compatibility and tumor–normal cell response under matched functional readouts, we further compared the viability responses of both normal HEK-293 cells and MCF-7 breast cancer cells following treatment with free DOX, UTM, UTMD and UTM + free DOX and corresponding concentrations of DOX (0, 12.5, 25, 50, 100, 200μg/mL) was added. Therefore, we employed the MTT assay to systematically investigate the effects of free DOX, UTM (containing an iron carrier), and UTMD (containing both an iron carrier and DOX) on the viability of human embryonic kidney HEK-293 cells and MCF-7 breast cancer cells. The cells were co-incubated with samples at various concentrations (0, 25, 50, 100, 200 μg/mL) under dark conditions for 24 hours, and the results are presented in Figure 6a and b.

The experimental results indicated that within the concentration range of 0–200 μg/mL, the free DOX group exhibited dose-dependent cytotoxicity, with cell viability decreasing from 100% to 62.0%. This behavior is consistent with the characteristics of conventional chemotherapy drugs.[88] By contrast, the UTM group maintained stable cell viability across all tested concentrations, remaining above 90%, which confirms its excellent biological inertness and favorable cytocompatibility toward normal cells.[89] Although the UTMD group, loaded with DOX, showed a moderate reduction in HEK-293 cell viability at high concentrations, cell survival still remained above 80%, indicating that the nanoplatform substantially alleviated the non-specific toxicity associated with free DOX exposure (Figure 6a).

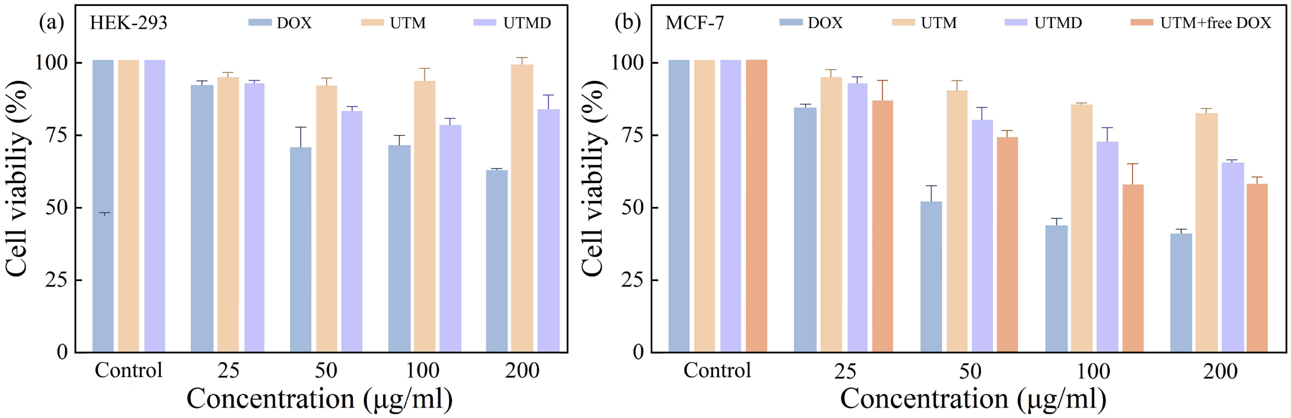

Figure 6 Comparative cytocompatibility evaluation of UTMD in MCF-7 tumor cells and HEK-293 normal cells under identical conditions. Cell viability following incubation (a) with free DOX, UTM, UTM+free DOX, and UTMD in MCF-7 cells, and (b) with free DOX, UTM, and UTMD in HEK-293 cells, demonstrating differential biological responses between tumor and normal cells and reduced nonspecific toxicity with carrier-mediated delivery.

To further determine whether this reduced toxicity in normal cells was accompanied by retained antitumor activity, additional viability assays were performed in MCF-7 cells under comparable treatment conditions. As shown in Figure 6b, UTM alone exhibited relatively low cytotoxicity, indicating that the carrier itself caused limited direct damage to tumor cells in the absence of DOX loading. Free DOX induced pronounced cytotoxicity in MCF-7 cells in a dose-dependent manner, while UTMD also produced evident viability reduction at elevated concentrations. Notably, the addition of the UTM + free DOX group showed cell viability levels between the free DOX and UTMD groups across all concentrations, indicating that the carrier mediated a gradual drug release, which resulted in reduced toxicity compared to free DOX but was still more toxic than UTMD alone. This suggests that the UTMD system, through controlled release, reduces the rapid cytotoxicity associated with free DOX while maintaining its therapeutic efficacy in cancer cells.

This differential response can be rationally associated with the microenvironment-responsive activation behavior of the UTMD nanoplatform. Compared with normal cells, tumor cells such as MCF-7 generally possess more acidic intracellular compartments and elevated GSH levels, which are more favorable for destabilizing the Fe-MOF shell and promoting responsive DOX release together with Fe-mediated redox perturbation. Under these tumor-relevant intracellular conditions, the UTMD system is more likely to induce oxidative imbalance through GSH depletion, ROS accumulation, and lipid peroxidation, thereby enhancing tumor cell vulnerability. In contrast, the relatively milder intracellular conditions in HEK-293 cells may reduce premature shell decomposition and oxidative activation, which helps explain the improved cytocompatibility observed in normal cells.

These findings provide critical evidence for the clinical translation of UTMD technology: 1) The nanocarrier carrier itself does not induce significant cell damage, meeting the safety standards for medical devices;[89] 2) The drug-loaded system maintains appreciable antitumor-associated cytotoxicity while reducing toxicity toward normal cells compared with free DOX, indicating a more favorable tumor–normal cell response profile and supporting the microenvironment-gated therapeutic rationale of the UTMD nanoplatform.[90,91]

Mechanistic Insights into Tumor-Activated Chemo–Ferroptosis Synergy

In this study, we explored the mechanistic synergy between chemotherapy and ferroptosis-associated oxidative damage facilitated by the UTMD nanoplatform. The core–shell UCNPs@TiO_2/Fe-MOF nanostructure harnesses a dual-responsive mechanism activated by the intracellular microenvironment, which promotes both DOX release and iron-mediated oxidative amplification. These coupled processes are proposed to enhance tumor cell susceptibility to redox-dependent damage beyond chemotherapy alone.

At the molecular level, the Fe-MOF component, specifically NH_2-MIL-88B(Fe), functions as a gatekeeping and redox-active layer, destabilizing under acidic and reducing intracellular conditions following cellular internalization. The release of iron ions from the Fe-MOF facilitates redox cycling and contributes to the generation of highly reactive ·OH

https://doi.org/10.2147/IJN.S604452

via Fenton-like reactions. These radicals, in turn, contribute to lipid peroxidation, a characteristic feature associated with ferroptosis, amplifying oxidative stress. In parallel, the elevated intracellular GSH concentration in tumor cells further participates in this process by accelerating Fe-MOF decomposition and Fe^{3+}/Fe^{2+} conversion, while the resulting GSH depletion weakens antioxidant defenses and exacerbates intracellular redox imbalance.

The Z-scheme heterojunction within the UCNPs@TiO_2/Fe-MOF nanoplatform may further strengthen this oxidative process by ensuring efficient charge separation, suppressing electron–hole recombination, and thereby boosting the overall redox activity. This energy band alignment between TiO_2 and NH_2-MIL-88B(Fe) is proposed to preserve both the reduction capability of electrons in TiO_2's CB and the oxidative potential of holes in NH_2-MIL-88B(Fe)'s VB. As a result, this configuration is expected to favor redox amplification and may help overcome the relatively limited efficiency of Fenton-like processes under biologically relevant conditions.

The iron redox cycle, coupled with the cytotoxic effects of DOX, triggers coordinated intracellular oxidative network characterized by GSH depletion, lipid peroxidation, and mitochondrial dysfunction (Figure 7), together with intracellular reactive oxygen species (ROS) accumulation. These biochemical and functional changes collectively support the occurrence of ferroptosis-associated oxidative damage in the UTMD-treated cells. Compared with conventional DOX delivery systems, the present architecture is therefore suggested to provide an additional redox-mediated therapeutic contribution beyond intracellular drug delivery alone.

Nevertheless, it should be noted that the present study does not include a structurally equivalent benchmark DOX nanocarrier lacking the Fe-MOF component. Therefore, the current mechanistic interpretation is based on indirect multi-parameter evidence rather than direct structural comparison. A limitation of this study is the lack of a benchmark DOX nanocarrier (eg, a non-iron or non-responsive control) for direct comparison of ferroptosis activation. Future work will systematically compare the UTMD platform with conventional nanocarriers to further validate the specific contribution of the Fe-MOF shell to ferroptosis-associated therapeutic efficacy. Future studies incorporating such benchmark

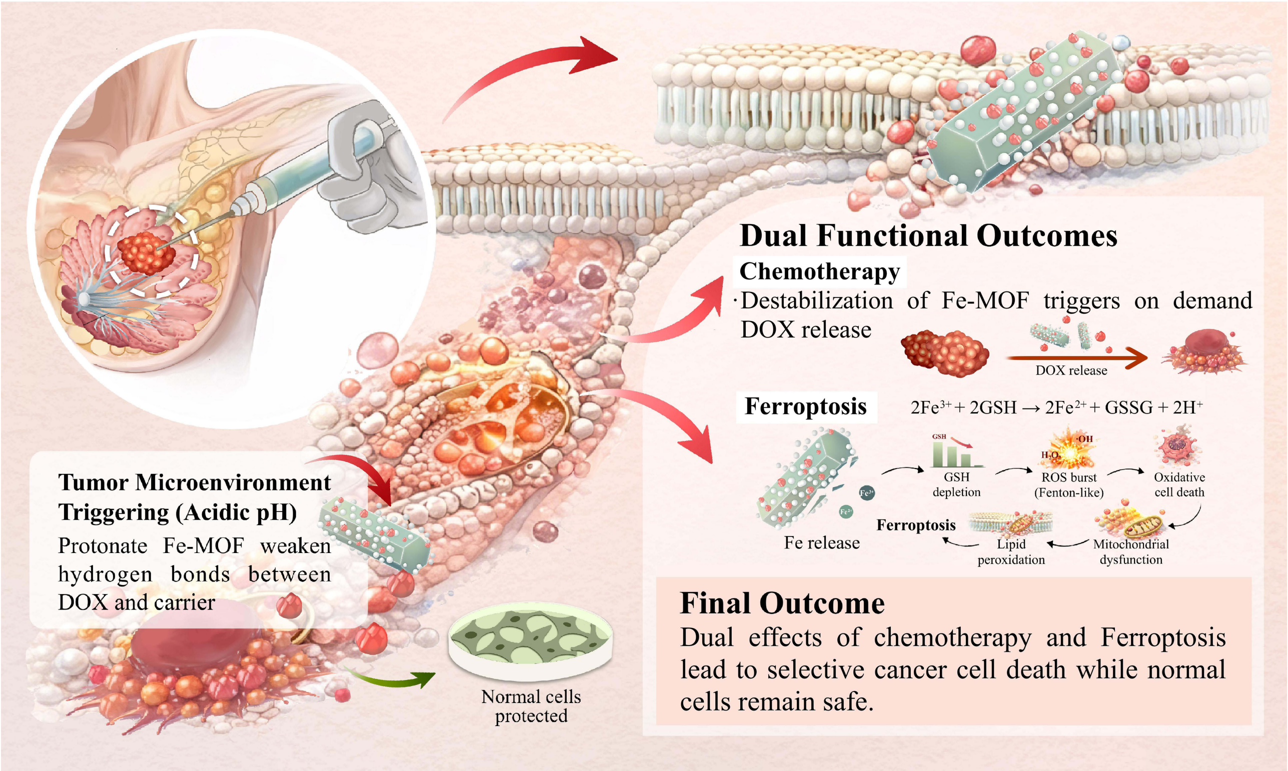

Figure 7 Schematic illustration of the microenvironment-activated chemo–ferroptosis mechanism of UTMD. The Fe-MOF gatekeeper undergoes pH/GSH-responsive destabilization, enabling intracellular DOX release and iron-driven oxidative amplification through GSH depletion, ROS generation, and lipid peroxidation.

nanocarrier controls would be valuable for further quantifying the specific contribution of the Fe-MOF shell to ferroptosis-associated therapeutic enhancement.

In summary, the UTMD nanoplatform utilizes a combination of chemotherapy and iron-mediated redox chemistry to induce ferroptosis-associated oxidative damage in tumor cells. This "one trigger–two outcomes" approach, which leverages intracellularly relevant cues such as acidic subcellular pH and elevated GSH, supports differential biological responses between cancerous and non-cancerous cells while reducing cytotoxicity toward normal cells.

More broadly, the present work can be positioned within the rapidly evolving framework of stimulus-responsive nanomedicine, particularly "targeting-by-activation" strategies in which therapeutic functions are conditionally triggered by biologically relevant cues rather than being constitutively active. Such approaches have increasingly been explored to improve therapeutic precision by coupling cargo function to disease-relevant biochemical environments rather than relying solely on passive accumulation or ligand-mediated recognition.[15,92] In recent years, this concept has been widely extended across diverse delivery systems, including inorganic and metal-ion-based nanoplatforms,[15,93,94] polymeric nanoparticle,[92,95] ionizable lipid nanoparticles (LNPs) for intracellular biomacromolecule delivery,[96,97] and cargo-engineered or programmable activation systems.[98,99] Within this broader context, the UTMD system is more appropriately interpreted as an intracellularly activated proof-of-concept nanoplatform that integrates responsive drug release with Fe-mediated redox perturbation under acidic and reducing intracellular conditions. Its conceptual distinction lies not merely in using a responsive carrier, but in coordinating chemotherapy release and ferroptosis-associated oxidative amplification through a shared activation logic, thereby offering a more mechanistically integrated design than conventional single-function delivery systems.

Nevertheless, the present findings remain limited to in vitro evaluation and should therefore be interpreted as a mechanistic proof-of-concept rather than definitive evidence of translational efficacy. Future in vivo studies will be essential to determine whether the proposed pH/GSH-responsive activation logic can effectively improve tumor selectivity, reduce off-target toxicity, and maintain favorable systemic behavior in complex biological environments. This will be particularly important because several recent activation-gated nanoplatforms have shown that in vitro-responsive behavior does not always directly translate into optimal in vivo biodistribution, tumor accumulation, or therapeutic index without careful structural and pharmacokinetic optimization. In particular, further validation of circulation stability, biodistribution, tumor accumulation, intracellular activation efficiency, and normal tissue safety will be required to more fully assess the translational potential of this strategy.

Conclusion

In conclusion, we have developed a novel intracellular microenvironment-responsive nanoplatform that integrates chemotherapy and ferroptosis through a pH/GSH-responsive core–shell structure UTMD. The system, consisting of an NH_2-MIL-88B(Fe) shell grown on UCNPs@TiO_2, functions as a dual "gatekeeper" that synchronizes the release of DOX with iron-induced oxidative amplification, implementing a "one trigger → two outcomes" chemo–ferroptosis strategy in MCF-7 breast cancer cells.

The system demonstrated excellent drug encapsulation efficiency (86.5%) and showed clear responsive release behavior under acidic and reducing buffered model conditions (43.2% at pH 5.0 and 60.3% at pH 6.0 + 10 mM GSH), while remaining relatively stable under physiological buffered conditions (16.1% at pH 7.4). This controlled release behavior supports microenvironment-responsive activation after cellular uptake rather than premature release under neutral buffered conditions, which is favorable for improving intracellular delivery precision while minimizing off-target effects.

Mechanistically, UTMD reshapes the intracellular redox environment, promoting GSH depletion and initiating iron-catalyzed Fenton reactions. The system's synergy between chemotherapy and ferroptosis was clearly evident through the substantial depletion of GSH (~45.4% reduction), a burst in ROS generation, and elevated lipid peroxidation, as measured by MDA levels. Importantly, UTMD also induced significant mitochondrial dysfunction, evidenced by MMP depolarization.

The UTMD nanoplatform demonstrated superior cytocompatibility compared to free DOX, maintaining over 80% cell viability in HEK-293 normal cells, in contrast to the 62% viability observed with free DOX at equivalent concentrations. Together with the matched viability response observed in MCF-7 cells, these findings highlight the potential of UTMD as a biocompatible and mechanistically interpretable nanoplatform that maintains antitumor-associated activity while reducing cytotoxicity toward normal cells in vitro. Overall, the present results support UTMD as an intracellularly responsive proof-of-concept nanoplatform for activation-gated chemo–ferroptosis therapy in breast cancer cell models.

Future studies will focus on validating the performance of this nanoplatform in more complex biological systems, particularly through in vivo evaluation of biodistribution, tumor accumulation, intracellular activation efficiency, and safety in normal tissues. Such investigations will be essential for further assessing the translational potential of this microenvironment-responsive chemo–ferroptosis strategy.

Data Sharing Statement

The data that support the findings of this study are available from the corresponding author, Baiqi Wang, upon reasonable request.

Acknowledgments

We would like to express our sincere gratitude to Ms. Wenqi Liu for her invaluable contributions and guidance throughout this project.

Author Contributions

All authors made a significant contribution to the work reported, whether that is in the conception, study design, execution, acquisition of data, analysis and interpretation, or in all these areas; took part in drafting, revising or critically reviewing the article; gave final approval of the version to be published; have agreed on the journal to which the article has been submitted; and agree to be accountable for all aspects of the work.

Funding

This work was supported by the National Natural Science Foundation of China (No. 82574048), the Joint Funds of the Natural Science Foundation of Tianjin (No. 25JCLZJC00240), and the Key Research Program of the Tianjin Municipal Education Commission (No. 2023ZD009).

Disclosure

The authors declare that they have no known competing financial interests or personal relationships that could have appeared to influence the work reported in this paper.

References

1. Niu Z, He J, Wang S, et al. Targeting glycolysis for treatment of breast cancer resistance: current progress and future prospects. *Int J Biol Sci*. 2025;21(6):2589–2605. doi:10.7150/ijbs.109803
2. Kim J, Harper A, McCormack V, et al. Global patterns and trends in breast cancer incidence and mortality across 185 countries. *Nat Med*. 2025;31(4):1154–1162. doi:10.1038/s41591-025-03502-3
3. Wu G-Y, Xiao M-Z, Hao W-C, et al. Drug resistance in breast cancer: mechanisms and strategies for management. *Drug Resist Updates*. 2025;83:101288. doi:10.1016/j.drup.2025.101288
4. Xiong X, Zheng L-W, Ding Y, et al. Breast cancer: pathogenesis and treatments. *Signal Transduction Targeted Ther*. 2025;10(1):49. doi:10.1038/s41392-024-02108-4
5. Roscigno G, Quintavalle C, Affinito A, et al. 2004P - Breast cancer organoids: a new tool for the prediction of drug penetration and patient outcome. *Annals Oncol*. 2019;30:v803–v804. doi:10.1093/annonc/mdz269.022
6. Saleem MZ, Huang R, Huang Y, et al. Targeting TRAP1-dependent metabolic reprogramming to overcome doxorubicin resistance in quiescent breast cancer. *Drug Resist Updates*. 2025;81:101226. doi:10.1016/j.drup.2025.101226
7. Ibrahim M, Abuwatfa WH, Awad NS, Sabouni R, Husseini GA. Encapsulation, release, and cytotoxicity of doxorubicin loaded in liposomes, micelles, and metal-organic frameworks: a review. *Pharmaceutics*. 2022;14:254.
8. Fang Y, Li C, Li X, et al. Harnessing boron-mediated Ti valence cycling in TiB_2-PEG-DOX: a multimodal CDT/PTT/CT platform for colorectal cancer therapy. *Small*. 2026;22(18):e14529. doi:10.1002/smll.202514529
9. Yin J, Zhang X, Yao W, et al. Tumor microenvironment-triggered intelligent nanoassemblies for fluorescence imaging activation and tumor-specific embolization therapy amplification. *Small*. 2025;21(38):e07309. doi:10.1002/smll.202507309

10. Wang Y, Yan T, Cai J, et al. A heterojunction-engineering nanodrug with tumor microenvironment responsiveness for tumor-specific cuproptosis and chemotherapy amplified sono-immunotherapy. *Biomaterials*. 2025;321:123319. doi:10.1016/j.biomaterials.2025.123319
11. Li R, Peng F, Cai J, et al. Redox dual-stimuli responsive drug delivery systems for improving tumor-targeting ability and reducing adverse side effects. *Asian J Pharmaceut Sci*. 2020;15(3):311–325. doi:10.1016/j.ajps.2019.06.003
12. Qin S, Zhao H-Y, Luo X-Y, et al. Photothermally reinforced nanozyme remodeling tumor microenvironment of redox and metabolic homeostasis to enhance ferroptosis in tumor therapy. *ACS Nano*. 2024;18(46):32235–32254. doi:10.1021/acsnano.4c13087
13. Xue-Hui S, Babalola KT, Heyns IM, et al. GSH-responsive prodrug-based nanodrugs for augmenting chemo-photodynamic synergistic therapy against tumors. *Nano Today*. 2024;57. doi:10.1016/j.nantod.2024.102368
14. Jianhua Z, Li Z, Zhu Y, et al. pH/GSH dual responsive nanosystem for nitric oxide generation enhanced type I photodynamic therapy. *Bioact Mat*. 2024;34. doi:10.1016/j.bioactmat.2023.12.023
15. Ehsani A, Fathi M, Goshtasbi H, et al. Zinc-cystine bio-MOF coated with folic acid-modified chitosan nanogel for targeted pH/glutathione dual-responsive drug delivery. *Int J Biolog Macromol*. 2025;321:146459. doi:10.1016/j.ijbiomac.2025.146459
16. Guang L, Zhuang L, Gan B. The roles of ferroptosis in cancer: tumor suppression, tumor microenvironment, and therapeutic interventions. *Cancer Cell*. 2024;42. doi:10.1016/j.ccell.2024.03.011
17. Huocheng Y, Yao X, Liu Y, Shen X, Li M, Luo Z. Ferroptosis nanomedicine: clinical challenges and opportunities for modulating tumor metabolic and immunological landscape. *ACS Nano*. 2023;17. doi:10.1021/acsnano.3c04632
18. Shiyao S, Xu S, Pang D. Emerging role of ferroptosis in breast cancer: New Dawn for overcoming tumor progression. *Pharmacol Therapeut*. 2022;232. doi:10.1016/j.pharmthera.2021.107992
19. Yu Z, Lepoitevin M, Serre C, et al. Iron-MOFs for biomedical applications. *Adv Healthcare Mat*. 2025;14(8):2402630. doi:10.1002/adhm.202402630
20. Wang M, Zhu M, Guan J, et al. Mixed-valent Fe-MOF accelerated Fe(III)/Fe(II) cycle for highly efficient photo-Fenton-like catalytic degradation of organic pollutants: Boosting mechanism and degradation pathways. *J Environ Chem Eng*. 2024;12(5):113577. doi:10.1016/j.jece.2024.113577
21. Wang Y, Pan Y, Sproules S, et al. Multifunctional Fe-Doped MOF-808 nanocomposites for chemo/chemodynamic synergistic therapy. *Small*. 2026;22(4):e12728. doi:10.1002/smll.202512728
22. Wang C, Sharma KS, Goo YT, et al. Structurally engineered ferrous metal–organic framework as a chemodynamic therapy nanoagent for concurrent hydroxyl radical and singlet oxygen generation. *Adv Funct Mat*. 2026:e29194. doi:10.1002/adfm.202529194.
23. Jingrong S, Xiao R, Wang T, et al. BRD4770 protects against DOX-induced cardiotoxicity by inhibiting apoptosis and ferroptosis. *Sci Adv*. 2025:11. doi:10.1126/sciadv.adw1720.
24. Huiru Z, Shan G, Liu M, et al. Harnessing ROS amplification and GSH depletion using a carrier-free nanodrug to enhance ferroptosis-based cancer therapy. *Small*. 2025;21. doi:10.1002/smll.202409250
25. Lucie H, Pini F, Soro LK, et al. Molecular upconversion nanoparticles for live-cell imaging. *ACS Nano*. 2025;19. doi:10.1021/acsnano.4c16762
26. Pengyu D, Gao K, Zhang L, et al. Hydrogen bond-assisted construction of MOF/semiconductor heterojunction photocatalysts for highly efficient electron transfer. *Appl Catalysis B*. 2024;357. doi:10.1016/j.apcatb.2024.124297
27. Wenyao D, Li B, Zhang W, et al. Two-photon responsive porphyrinic metal-organic framework involving Fenton-like reaction for enhanced photodynamic and sonodynamic therapy. *J Nanobiotechnol*. 2022;20. doi:10.1186/s12951-022-01436-3
28. Shuang L, Xiao X, Bai L, et al. Conferring Ti-Based MOFs with defects for enhanced sonodynamic cancer therapy. *Adv Mat*. 2021;33. doi:10.1002/adma.202100333
29. Ren H, Bai R, Liu C, et al. Quantitative evaluation for the contribution of each component in $NaYF_4$: yb, Tm@$NaYF_4$: yb, Ho@$NaYF_4$ upconversion nanoparticle: active shell, inert shell, size, and their cooperation. *J Luminescence*. 2023;263:120057. doi:10.1016/j.jlumin.2023.120057
30. Zhang X, Sun H, Huang J, et al. Alkalized MXene-supported nanoscale zero-valent iron in situ derived from NH_2-MIL-88B(Fe) for the highly efficient catalytic reduction of 4-nitrophenol. *Mat Today Sustainab*. 2022;18:100145. doi:10.1016/j.mtsust.2022.100145
31. Ding M, Yin S, Chen D, et al. Hexagonal $NaYF_4$:Yb^{3+}/Er^{3+} nano/micro-structures: controlled hydrothermal synthesis and morphology-dependent upconversion luminescence. *Appl Surf Sci*. 2015;333:23–33. doi:10.1016/j.apsusc.2015.01.240
32. Challagulla S, Tarafder K, Ganesan R, et al. Structure sensitive photocatalytic reduction of nitroarenes over TiO_2. *Scient Rep*. 2017;7(1):8783. doi:10.1038/s41598-017-08599-2
33. Jia L, Ye H, Zeng X, et al. Triphase photocatalytic hydrogel for molecule oxygen activation with enhanced interfacial electric field by Ti-O-Fe bridging bond. *J Hazardous Mat*. 2025;494:138490. doi:10.1016/j.jhazmat.2025.138490
34. Li J, Zhang B, Liu P, et al. Hierarchically porous MOF@COF structures with ultrafast gas diffusion rate for C_2H_6/C_2H_4 separation. *J Colloid Interface Sci*. 2024;669:258–264. doi:10.1016/j.jcis.2024.04.227
35. Feizpoor S, Habibi-Yangjeh A, Luque R, et al. Preparation of TiO_2/Fe-MOF n–n heterojunction photocatalysts for visible-light degradation of tetracycline hydrochloride. *Chemosphere*. 2023;336:139101. doi:10.1016/j.chemosphere.2023.139101
36. Bhattacharjee A, Purkait MK, Gumma S, et al. Doxorubicin loading capacity of MIL-100(Fe): effect of synthesis conditions. *J Inorg Organometal Polymers Mat*. 2020;30(7):2366–2375. doi:10.1007/s10904-020-01456-2
37. Yan H, Dong J, Luan X, et al. Ultrathin porous nitrogen-doped carbon-coated CuSe heterostructures for combination cancer therapy of photothermal therapy, photocatalytic therapy, and logic-gated chemotherapy. *ACS Appl Mat Interfaces*. 2022;14(50):56237–56252. doi:10.1021/acsami.2c12503
38. Guo D, Lin Q, Liu N, et al. Copper-based metal–organic framework co-loaded doxorubicin and curcumin for anti-cancer with synergistic apoptosis and ferroptosis therapy. *Int J Pharmaceut*. 2024;666:124744. doi:10.1016/j.ijpharm.2024.124744
39. Tang J, Zhang R, Guo M, et al. Nucleosome-inspired nanocarrier obtains encapsulation efficiency enhancement and side effects reduction in chemotherapy by using fullerenol assembled with doxorubicin. *Biomaterials*. 2018;167:205–215. doi:10.1016/j.biomaterials.2018.03.015
40. Cai K, He X, Song Z, et al. Dimeric drug polymeric nanoparticles with exceptionally high drug loading and quantitative loading efficiency. *J Am Chem Soc*. 2015;137(10):3458–3461. doi:10.1021/ja513034e
41. Pasban S, Raissi H. PNIPAM/Hexakis as a thermosensitive drug delivery system for biomedical and pharmaceutical applications. *Scient Rep*. 2022;12(1):14363. doi:10.1038/s41598-022-18459-3

42. Wang L, Xu Y, Liu C, et al. Copper-doped MOF-based nanocomposite for GSH depleted chemo/photothermal/chemodynamic combination therapy. *Chem Eng J*. 2022;438:135567. doi:10.1016/j.cej.2022.135567
43. Chen H-Y, Xu H-B, Lv J, et al. Smart nanoplatform for visualizing hydrogen sulfide and amplifying oxidative stress to tumor apoptosis. *ACS Sensors*. 2023;8(9):3555–3562. doi:10.1021/acssensors.3c01203
44. Hou M, Liu M, Yu H, et al. Spatially asymmetric nanoparticles for boosting ferroptosis in tumor therapy. *Nano Lett*. 2024;24(4):1284–1293. doi:10.1021/acs.nanolett.3c04293
45. Chen S, Yan Y, Chen Y, et al. All-in-one HN@Cu-MOF nanoparticles with enhanced reactive oxygen species generation and GSH depletion for effective tumor treatment. *J Mat Chem B*. 2023;11(48):11519–11531. doi:10.1039/D3TB02433D
46. Xing L, Liu X-Y, Zhou T-J, et al. Photothermal nanozyme-ignited Fenton reaction-independent ferroptosis for breast cancer therapy. *J Controlled Rel*. 2021;339:14–26. doi:10.1016/j.jconrel.2021.09.019
47. Kawano I, Adamcova M. MicroRNAs in doxorubicin-induced cardiotoxicity: the DNA damage response. *Front Pharmacol*. 2022;13. doi:10.3389/fphar.2022.1055911.
48. Shi Y, Chang L, Pan C, et al. Biodegradable hollow mesoporous bimetallic nanoreactors to boost chemodynamic therapy. *J Colloid Interface Sci*. 2024;656:93–103. doi:10.1016/j.jcis.2023.11.086
49. Li X, Pan J, Li Y, et al. Development of a localized drug delivery system with a step-by-step cell internalization capacity for cancer immunotherapy. *ACS Nano*. 2022;16(4):5778–5794. doi:10.1021/acsnano.1c10892
50. Thakur CK, Martins FG, Karthikeyan C, et al. In silico-guided discovery and in vitro validation of novel sugar-tethered lysinated carbon nanotubes for targeted drug delivery of doxorubicin. *J Mol Model*. 2024;30(8). doi:10.1007/s00894-024-06061-5
51. Rastogi S, Ansari MN, Saeedan AS, et al. Novel furan chalcone modulates PHD-2 induction to impart antineoplastic effect in mammary gland carcinoma. *J Biochem Mol Toxicol*. 2024;38(4):e23679. doi:10.1002/jbt.23679
52. Ullah I, Khalil AT, Zia A, et al. Insight into the molecular mechanism, cytotoxic, and anticancer activities of phyto-reduced silver nanoparticles in MCF-7 breast cancer cell lines. *Microscopy Res Techn*. 2024;87(7):1627–1639. doi:10.1002/jemt.24540
53. Li Q, Wang F, Shi L, et al. Nanotrains of DNA copper nanoclusters that triggered a cascade fenton-like reaction and glutathione depletion to doubly enhance chemodynamic therapy. *ACS Appl Mat Interfaces*. 2022;14(33):37280–37290. doi:10.1021/acsami.2c05944
54. He Y, Tian X, Zhang M, et al. Fenton-like nanoparticles capable of H 2 O 2 self-supply and glutathione consumption for chemodynamic and chemotherapy of cancer. *Biomater Sci*. 2024;12(21):5534–5546. doi:10.1039/D4BM00930D
55. T CSL, Zhao XH, Zhou S, et al. Correction to “LncRNA LIMp27 regulates the DNA damage response through p27 in p53-Defective cancer cells”. *Adv Sci*. 2025;12(10):2500857. doi:10.1002/advs.202500857
56. Yang P, Zhang J, Chang Y, et al. Tumor microenvironment responsive smart nanoplatform for synergistic tumor therapy through co-enhancement of GSH depletion and hypoxia relief. *J Inorg Biochem*. 2025;272:113005. doi:10.1016/j.jinorgbio.2025.113005
57. Ma X, Xu M, Zhang X, et al. Gambogenic acid inhibits proliferation and ferroptosis by targeting the miR-1291/FOXA2 and AMPKα/SLC7A11/GPX4 axis in colorectal cancer. *Cell Biol Int*. 2023;47(11):1813–1824. doi:10.1002/cbin.12072
58. Wang Y, Zheng G, Li X, et al. A dual-function hyaluronic acid-encapsulated nanoplatform enables triple GSH depletion for apoptosis-ferroptosis synergistic oncotherapy. *Int J Biol Macromol*. 2025;308:142650. doi:10.1016/j.ijbiomac.2025.142650
59. Huang L, Zhu J, Xiong W, et al. Tumor-generated reactive oxygen species storm for high-performance ferroptosis therapy. *ACS Nano*. 2023;17(12):11492–11506. doi:10.1021/acsnano.3c01369
60. Li S, Wang B, Tao J, et al. Chemodynamic therapy combined with endogenous ferroptosis based on “sea urchin-like” copper sulfide hydrogel for enhancing anti-tumor efficacy. *Int J Pharmaceut*. 2024;660:124330. doi:10.1016/j.ijpharm.2024.124330
61. Meng Y, Zhang D, Song Y, et al. Precisely designed Fe $_x$ ($_x$ = 1–2) cluster nanocatalysts for effective nanocatalytic tumor therapy. *Nanoscale*. 2023;15(5):2305–2315. doi:10.1039/D2NR05869C
62. Lee Y-B, Shin H-W, Shrestha S, et al. Ferroptosis in neutrophils. *J Leukocyte Biol*. 2025;117(5). doi:10.1093/jleuko/qiaf039
63. La Sala L, Pontiroli AE. Correction: la Sala et al. New fast acting glucagon for recovery from hypoglycemia, a life-threatening situation: nasal powder and injected stable solutions. *Int J Mol Sci*. 2023;24:5625. doi:10.3390/ijms24065625
64. Meng X, Varol O, Barabási A-L, et al. Hidden citations obscure true impact in science. *PNAS Nexus*. 2024;3(5):pgae155. doi:10.1093/pnasnexus/pgae155
65. Gorenshtein A, Shihada K, Sorka M, et al. LITERAS: Biomedical literature review and citation retrieval agents. *Computers Biol Med*. 2025;192:110363. doi:10.1016/j.compbiomed.2025.110363
66. Frandsen TF, Eriksen MB. Supplementary strategies identified additional eligible studies in qualitative systematic reviews. *J Clin Epidemiol*. 2023;159:85–91. doi:10.1016/j.jclinepi.2023.04.017
67. Xue X, Wang M, Cui J, et al. Glutathione metabolism in ferroptosis and cancer therapy. *Cancer Lett*. 2025;621:217697. doi:10.1016/j.canlet.2025.217697
68. Campos J, Gleitze S, Hidalgo C, et al. IP3R-mediated calcium release promotes ferroptotic death in SH-SY5Y neuroblastoma cells. *Antioxidants*. 2024;13(2):196. doi:10.3390/antiox13020196
69. Zhang J, Zhang S, Liu M, Yang Z, Huang R. Research progress on ferroptosis and nanotechnology-based treatment in triple-negative breast cancer. *Breast Cancer*. 2024;16:347–358. doi:10.2147/bctt.S475199
70. Sun R, Ma W, Ling M, et al. pH-activated nanoplatform for visualized photodynamic and ferroptosis synergistic therapy of tumors. *J Controlled Release*. 2022;350:525–537. doi:10.1016/j.jconrel.2022.08.050
71. Wang X, Zhao L, Wang C, et al. Potent nanoreactor-mediated ferroptosis-based strategy for the reversal of cancer chemoresistance to Sorafenib. *Acta Biomat*. 2023;159:237–246. doi:10.1016/j.actbio.2023.01.053
72. Teng Y, Huang Y, Tao X, et al. Emerging role of ferroptosis in ultraviolet radiation-driven skin photoaging: a narrative review. *Photochem Photobiolog Sci*. 2025;24(3):531–542. doi:10.1007/s43630-025-00691-1
73. Zheng J, Liu Y, Zhu F, et al. Picropodophyllin induces ferroptosis via blockage of AKT/NRF2/SLC7A11 and AKT/NRF2/SLC40A1 axes in hepatocellular carcinoma as a natural IGF1R inhibitor. *Phytomedicine*. 2025;143:156840. doi:10.1016/j.phymed.2025.156840
74. Ma C, Hu H, Liu H, et al. Lipotoxicity, lipid peroxidation and ferroptosis: a dilemma in cancer therapy. *Cell Biol Toxicol*. 2025;41(1). doi:10.1007/s10565-025-10025-7

75. Parul G, Sharma A, Sachin, Sharma S, Sharma D. Phytoconstituents-mediated targeting of ferroptosis for the treatment of cardiovascular disease. *Current Cardiol Rev*. 2026;22(1):156–171. doi:10.2174/011573403X370981250618074406
76. Tang C, Liu K, Gao X, et al. A metal-organic framework functionalized CaO_2^-based cascade nanoreactor induces synergistic cuproptosis/ ferroptosis and Ca^{2+} overload-mediated mitochondrial damage for enhanced sono-chemodynamic immunotherapy. *Acta Biomaterial*. 2025;193:455–473. doi:10.1016/j.actbio.2024.12.010
77. Xu B, Ding Z, Hu Y, et al. Preparation and evaluation of the cytoprotective activity of micelles with DSPE-PEG-C60 as a carrier against doxorubicin-induced cytotoxicity. *Front Pharmacol*. 2022;13. doi:10.3389/fphar.2022.952800
78. Xue X-B, Lv T-M, Hou J-Y, et al. Vibsane-type diterpenoids from Viburnum odoratissimum inhibit hepatocellular carcinoma cells via the PI3K/ AKT pathway. *Phytomedicine*. 2023;108:154499. doi:10.1016/j.phymed.2022.154499
79. Tang -Q-Q, Wang Z-D, An X-H, et al. Apigenin ameliorates H_2O_2-Induced oxidative damage in melanocytes through nuclear factor-E2-Related Factor 2 (Nrf2) and Phosphatidylinositol 3-Kinase (PI3K)/Protein Kinase B (Akt)/Mammalian Target of Rapamycin (mTOR) pathways and reducing the generation of reactive oxygen species (ROS) in Zebrafish. *Pharmaceuticals*. 2024;17(10):1302. doi:10.3390/ph17101302
80. Parisi K, McKenna JA, Lowe R, et al. Hyperpolarisation of mitochondrial membranes is a critical component of the antifungal mechanism of the plant defensin, Ppdef1. *J Fungi*. 2024;10(1):54. doi:10.3390/jof10010054
81. Venkatappa MM, Udagani C, Hanume Gowda SM, et al. Green synthesised TiO_2 nanoparticles-mediated terenna asiatica: evaluation of their role in reducing oxidative stress, inflammation and human breast cancer proliferation. *Molecules*. 2023;28(13):5126. doi:10.3390/molecules28135126
82. Vera MJ, Ponce I, Almarza C, et al. CCL2 and lactate from chemotherapeutics-treated fibroblasts drive malignant traits by metabolic rewiring in low-migrating breast cancer cell lines. *Antioxidants*. 2024;13(7):801. doi:10.3390/antiox13070801
83. Gibb Z, Aitken RJ, Sheridan AR, et al. The effects of oxidative stress and intracellular calcium on mitochondrial permeability transition pore formation in equine spermatozoa. *FASEB BioAdv*. 2024;6(6):143–158. doi:10.1096/fba.2023-00051
84. Xiao Y, Wan J, Gao X, et al. Versatile fluorescence lifetime-based copper probe to quantify mitochondrial membrane potential and reveal its interaction with protein aggregation. *Anal Chem*. 2024;96(16):6493–6500. doi:10.1021/acs.analchem.4c00909
85. Peng F, Ai X, Sun J, et al. Fluorescence lifetime super-resolution imaging unveil the dynamic relationship between mitochondrial membrane potential and cristae structure using the förster resonance energy transfer strategy. *Anal Chem*. 2024;96(27):11052–11060. doi:10.1021/acs.analchem.4c01905
86. Wang R, Liu L, Min L, et al. Mitochonic Acid 5 increases ram sperm quality by improving mitochondrial function during storage at 4 °C. *Animals*. 2024;14(3):368. doi:10.3390/ani14030368
87. Wang H, Li C, Zhu L, et al. Adiponectin attenuates H_2O_2-induced apoptosis in chicken skeletal myoblasts through the lysosomal-mitochondrial axis. *In Vitro Cell Dev Biol Animal*. 2024;60(7):805–814. doi:10.1007/s11626-024-00857-8
88. Mathur R, Suarez JI. Coagulopathy in isolated traumatic brain injury: myth or reality. *Neurocrit Care*. 2022;38(2):429–438. doi:10.1007/s12028-022-01647-4
89. Samani SS, Sameiyan E, Tabatabaei Yazdi F, et al. Sandwich-type aptamer-based biosensors for thrombin detection. *Anal Meth*. 2024;16 (14):1985–2001. doi:10.1039/D3AY02196C
90. Li SC. Mastering the craft: creating an insightful and widely-cited literature review. *World J Stem Cells*. 2023;15(8):781–786. doi:10.4252/wjsc.v15.i8.781
91. Rowland DL, Tamas S, Hevesi K, et al. Updating, correcting, and calibrating the narrative about premature ejaculation. *Sex Med Rev*. 2024;12 (3):401–410. doi:10.1093/sxmrev/qeae036
92. Ding X, Yu W, Wan Y, et al. A pH/ROS-responsive, tumor-targeted drug delivery system based on carboxymethyl chitin gated hollow mesoporous silica nanoparticles for anti-tumor chemotherapy. *Carbohydrate Polymers*. 2020;245:116493. doi:10.1016/j.carbpol.2020.116493
93. Duan F, Feng X, Yang X, et al. A simple and powerful co-delivery system based on pH-responsive metal-organic frameworks for enhanced cancer immunotherapy. *Biomaterials*. 2017;122:23–33. doi:10.1016/j.biomaterials.2017.01.017
94. Qian M, Jiang G, Guo W, et al. A biodegradable nanosuspension locally used for inhibiting postoperative recurrence and brain metastasis of breast cancer. *Nano Lett*. 2024;24(10):3165–3175. doi:10.1021/acs.nanolett.3c05146
95. Xu X, Wu J, Liu Y, et al. Ultra-pH-responsive and tumor-penetrating nanoplatform for targeted siRNA delivery with robust anti-cancer efficacy. *Angewandte Chemie Int Ed*. 2016;55(25):7091–7094. doi:10.1002/anie.201601273
96. Kim J, Jozic A, Lin Y, et al. Engineering lipid nanoparticles for enhanced intracellular delivery of mRNA through inhalation. *ACS Nano*. 2022;16 (9):14792–14806. doi:10.1021/acsnano.2c05647
97. Fu L, Hua X, Jiang X, et al. Multistage systemic and cytosolic protein delivery for effective cancer treatment. *Nano Lett*. 2022;22(1):111–118. doi:10.1021/acs.nanolett.1c03293
98. Liang Z, Tan K, Yin Li C, et al. Self-feedback loop-containing synthetic mRNA switches for controlled microRNA sensing. *Bioorg Chem*. 2024;144:107081. doi:10.1016/j.bioorg.2023.107081
99. Masaki K, Fujita Y, Saito H, et al. MicroRNA-responsive ON-OFF hybrid mRNA switch for precise protein expression control. *Mol Ther Nucleic Acids*. 2025;36(3):102609. doi:10.1016/j.omtn.2025.102609